DTU Library

Effect of Lateral and Stress-Dependent Viscosity Variations on GIA Induced Uplift Rates in the Amundsen Sea Embayment

Blank, B.; Barletta, V.; Hu, H.; Pappa, F.; van der Wal, W.

Key Points:
- Uplift rates in the Amundsen Sea Embayment since 1900 are modeled with lateral and stress-dependent viscosity changes (composite rheology)
- Including stresses from earlier ice loads can both increase and decrease stress-induced viscosity changes
- 1D and 3D model uplift cannot be distinguished between using GPS sites but modeled uplift show significant differences in high uplift areas

Effect of Lateral and Stress-Dependent Viscosity Variations on GIA Induced Uplift Rates in the Amundsen Sea Embayment

B. Blank[1] , **V. Barletta[2]** , **H. Hu[3]** , **F. Pappa[4]** , and **W. van der Wal[1]**

[1]Delft University of Technology, Delft, The Netherlands, [2]University of Technology Denmark, Kongens Lyngby, Denmark, [3]Imperial College London, London, England, [4]Kiel University, Kiel, Germany

Abstract Accurate glacial isostatic adjustment (GIA) models are required for correcting measurements of mass change in Antarctica and for improving knowledge of the sub-surface, especially in areas of large current ice loss such as the Amundsen Sea Embayment (ASE). Regionally, seismic and gravity data suggests lateral differences in viscosity (3D). Furthermore, mantle flow laws allow for a stress-dependent effective viscosity which changes over time (3D-s). In this study we investigate whether models with 3D/3D-s have significant effects on the uplift in the region. We use a finite element model with composite rheology consisting of diffusion and dislocation creep, forced by an ice deglaciation model starting in 1900. We use its uplift predictions as synthetic observations to test the performance of 1D model inversion in the presence of viscosity variations. Stress-dependent rheology results in lower viscosity beneath the load and a more localized uplift pattern. We demonstrate that the background stress from earlier ice load changes can both increase or decrease the influence of stress-induced effective viscosity changes. For the ASE, fitting 1D models to 3D model uplift results in a best fitting model with viscosity that represents the average of a large area, while for 3D-s rheology, local viscosity is more influential. 1D models are statistically indistinguishable from 3D/3D-s viscosity with current GPS stations. However, 3D and 3D-s models should be taken into account when accurate uplift and gravity rate patterns are needed, as uplift can differ up to 45% compared to 1D models in between existing GPS stations.

Plain Language Summary The Amundsen Sea Embayment (ASE) is a region in West-Antarctica, which is losing mass upstream of the grounding line faster than almost any other region. Measurements of current ice mass change are obscured by uplift due to the melting of ice sheets in that past, termed glacial isostatic gdjustment (GIA). An accurate GIA model is required. The state-of-the-art GIA model for the region assumes that the viscosity depth profile is the same everywhere. However, effective viscosity can change with location and under influence of stress which changes over time. In this study we use a finite element model to simulate GIA in the ASE and compare the simulated uplift from these models to an inverted 1D model. We show that when estimating average mantle viscosities, a simpler model would suffice. When higher stresses due to rapid deglaciation are taken into account in the description of the mantle flow, the uplift at the point of rapid deglaciation has a stronger rebound effect than previously considered. This would mean that the local ice mass loss obtained after correcting with current GIA models might also be bigger than what is obtained after correcting with simpler GIA models.

1. Introduction

Glacial isostatic adjustment (GIA) is the response of the solid Earth to the melting of large ice sheets, and the accompanying changes in the relative sea level, and gravitational field. It is ongoing in areas of former large Pleistocene ice sheets such as North America and Scandinavia, but also in currently glaciated areas such as Antarctica. There, modeling of GIA is necessary to correct satellite measurements of mass change for GIA in order to reveal current ice mass change (Caron & Ivins, 2020; King et al., 2010; Shepherd et al., 2018). Additionally, comparing output of GIA models to observations that are dominated by GIA or corrected for current ice mass change effects can give us insight in the structure of the Earth. GIA is sensitive to a viscosity distribution in radial direction, but also in lateral directions. This is particularly relevant in Antarctica, where it is known that a large contrast in viscosity between East and West Antarctic mantle exists. Furthermore, GIA plays an important role in the deglaciation process itself through a feedback loop

of the solid-earth response with the Antarctic ice sheet (Barletta et al., 2018; Gomez et al., 2018; Whitehouse et al., 2019). Still 1D models, which can be described as models that only have radially varying parameters (Ivins et al., 2013; Peltier, 2004; Whitehouse et al., 2012), have mostly been used to correct satellite gravimetry measurements (King et al., 2010; Shepherd et al., 2018) because of their computational simplicity. 1D models have also been used to model small regions in West Antarctica which have lower than average viscosity (Nield et al., 2014; Samrat et al., 2020; Wolstencroft et al., 2015).

GIA induced uplift rate and horizontal rate is altered when using 3D rheology (A et al., 2013; Kaufmann et al., 2005; Nield et al., 2018; van der Wal et al., 2015), especially near the boundary between low viscosities in West Antarctica and high viscosities in East Antarctica. In Kaufmann et al. (2005) a 3D model was used to investigate the effects of lateral viscosity variations in the Antarctic mantle. While the results of Kaufmann et al. (2005) showed that their 3D Maxwell rheology has some influence on GIA (most notably horizontal motion), they concluded that the differences in ice models have a larger impact. A et al. (2013) showed that a compressible 3D rheology affects GIA model uplift predictions to a large degree in Antarctica (up to 60%), although it must be noted this figure was found when the 3D rheology was compared to a continent wide average viscosity. The differences for the Amundsen Sea Embayment (ASE) specifically were negligible. However, as these studies were not focused on finding accurate rheology parameters or quantifying rheology differences in terms of GIA movement, both Kaufmann et al. (2005) and A et al. (2013) tested a single set of 3D rheology parameters and used ice models that did not incorporate the recent ice loss in the ASE. It is shown by van der Wal et al. (2015) using multiple different sets of rheology parameters that the effect of unknown lateral viscosity changes can be larger than these previous studies suggested. This raises the question under what condition 3D viscosity variations become significant.

The Amundsen Sea Embayment (ASE) exhibits the largest observed ice mass loss of the Antarctic continent in the last few decades (Rignot et al., 2019; Shepherd et al., 2018, 2019) of about −130 Gt/y (Barletta et al., 2018). A destabilization of the Amundsen glaciers could start a collapse of the whole West Antarctic ice sheet (Seroussi et al., 2017) even though solid earth response could provide a positive feedback that acts to slow down the acceleration of ice melt (Konrad et al., 2015). The largest ice loss currently occurs at the Pine Island Glacier (PIG), the glaciers near the Crosson Ice shelf and at the Thwaites Glacier (TG; Gourmelen et al., 2018; Konrad et al., 2016). The ASE is the region where the highest uplift is measured by means of GPS stations. Only a small part of the uplift rates is explained by the elastic response of present-day melt, which indicates that the region either has an ice history in which large Pleistocene or early Holocene loads were present or it is underlain by a low viscosity which makes it more sensitive to more recent ice load changes. Global or large scale GIA models (Martín-Español et al., 2016; Nield et al., 2018; either 3D or 1D) are unlikely to included recent ice mass losses to a high temporal resolution and are therefore unable to predict the GPS measured uplift values observed in the ASE because they do not model the deglaciation in the last century. Barletta et al. (2018) demonstrated with a 1D model that the ice loss of the last few decades in combination with a low viscosity is necessary to explain the high uplift values.

In Barletta et al. (2018), a good fit was achieved between GPS data and simulations with a GIA model in which viscosity only varies in radial direction. However, seismic models suggest lateral changes in Earth properties below or near the region (An et al., 2015a; Lloyd et al., 2015) but it is not clear if these viscosity contrasts have significant effects on the uplift rate. Furthermore, it is not clear whether the viscosities found for the ASE by means of a 1D model are a good representation of the average 3D viscosity, and whether inferences from 1D models can be used as local constraints on 3D viscosity maps. Viscosity is a macroscopic description of deformation that takes place at micro-scale. Experiments on mantle rocks show different deformation mechanisms which depend on the grain size of the rock, but also mechanisms which depend on stress with an exponent larger than one (Hirth & Kohlstedt, 2003). Such behavior is also called power-law creep. Because of the non-linear stress dependence effective viscosity decreases as stress increases. This could lead to further stress changes and changes in effective viscosity.

Nield et al. (2018) showed that the use of a representative 1D model may not only affect the magnitude of the GIA uplift compared to 3D non-linear rheology, but also the uplift gradient in their GIA uplift profile. Non-linear rheology results in steeper gradient and makes the pattern more localized. More recently there have even been efforts through the combination of multiple 1D models, to simulate 3D lateral differences in Earth structure. In Hartmann et al. (2020) Antarctica was modeled by different 1D models for the Eastern

and Western parts of the continent. The results showed large conformity with the 3D finite volume model used in Hay et al. (2017). Finally, in Powell et al. (2020) a direct comparison is made between 3D models and 1D models for Antarctica and West Antarctica specifically. Their conclusion is that introducing lateral viscosity differences lead to measurable differences in horizontal bedrock movement and smaller differences in the vertical component for the stations in ASE at present day. However, there is strong emphasis on recent ice mass solely which leaves the question how past changes in both ice loading and Earth parameters would affect their conclusions.

Using power-law rheology the viscosity becomes stress-dependent, with higher stresses causing lower viscosity. Therefore, large ice mass changes and the subsequent stress changes can lower local viscosity. Furthermore, in a power-law rheology viscosity is also dependent on background stresses (Gasperini et al., 1992; Schmeling, 1987; Wu, 2001). Processes such as mantle convection, post-seismic deformation, and stresses from earlier ice loads could contribute to the total stress in the mantle and could change the effective viscosity. To express the fact that steady-state effective viscosity changes with location and under influences of stress (Von Mises stress, specifically), which is itself is dependent on time, we will use the term 3D-s viscosity, or even 3D-s model, which means a model with laterally varying and stress-dependent viscosity. Stress-dependent models are not widely considered when computing GIA corrections although the effective viscosity can change in time by up to two orders of magnitude in viscosity (Barnhoorn et al., 2011). A GIA model with stress-dependent viscosity has been used for Antarctica (van der Wal et al., 2015), but for the ASE there has been no study detailing the effect on non-linear rheology, and the effect from background stress.

While stress-dependence can lead to effective viscosity that changes in time, it is not the same as transient rheology in which the solid Earth response is dependent on the loading frequency. The (extended) Burgers rheology is a notable example of a rheology that includes transient creep (Ivins et al., 2020; Jackson & Faul, 2010), It is used for example for post-seismic deformation (Nield et al., 2020) and seismic wave response (Carcione et al., 2014). It is possible that the response of the loading to ice load changes since is also governed by transient creep. Lau and Holtzman (2019) place different rheologies in one frame-work that can be used for different geodynamics processes. However, here we focus on the Maxwell model that combines elastic and viscous response, with the viscous response taken to be steady-state non-linear creep, with creep properties that can vary with location.

We identified the following research question: *What is the influence of 3D/3D-s effective viscosity profiles in GIA models on uplift rates in the Amundsen Sea Sector?* This question is divided into the following sub-questions:

1. How representative is the best fitting viscosity in a 1D Earth model of average 3D viscosity?
2. Can 3D viscosity be discerned in a statistical significant manner from 1D models using current uplift rate measurements?
3. How important is stress-dependent viscosity for the uplift?
4. What is the influence of background stresses on 3D-s effective viscosity and uplift?

In this study we will use 3D and 3D-s GIA models to simulate uplift rates at GPS station locations. The simulated GPS values will be used to perform an inversion for viscosity in a 1D model, similar to van der Wal et al. (2015). The best fitting 1D viscosities found will be compared to an average of the local 3D viscosities. This will provide insight in whether the best-fitting 1D viscosity model is an average of the 3D model, or whether 1D samples the 3D viscosities in a different way. Furthermore, we will also investigate the uplift pattern of the 3D and 3D-s models and see to what extent they can be represented by a 1D model. Finally, a comparison will be made between 3D and 3D-s models to study the effects of the stress-dependent viscosity. Here we also include a full glacial history to investigate whether the background stresses in the mantle due to earlier deglaciation influence our findings for the recent ice-load changes.

The structure of this paper is as follows. In Section 2, we will start by introducing the FE model. After that, we will describe Earth model parameters and ice input for the model. This will be followed by a short description of the 1D model used for the inversion. In Section 3, the research questions are addressed, after which main conclusions are summarized in the last section.
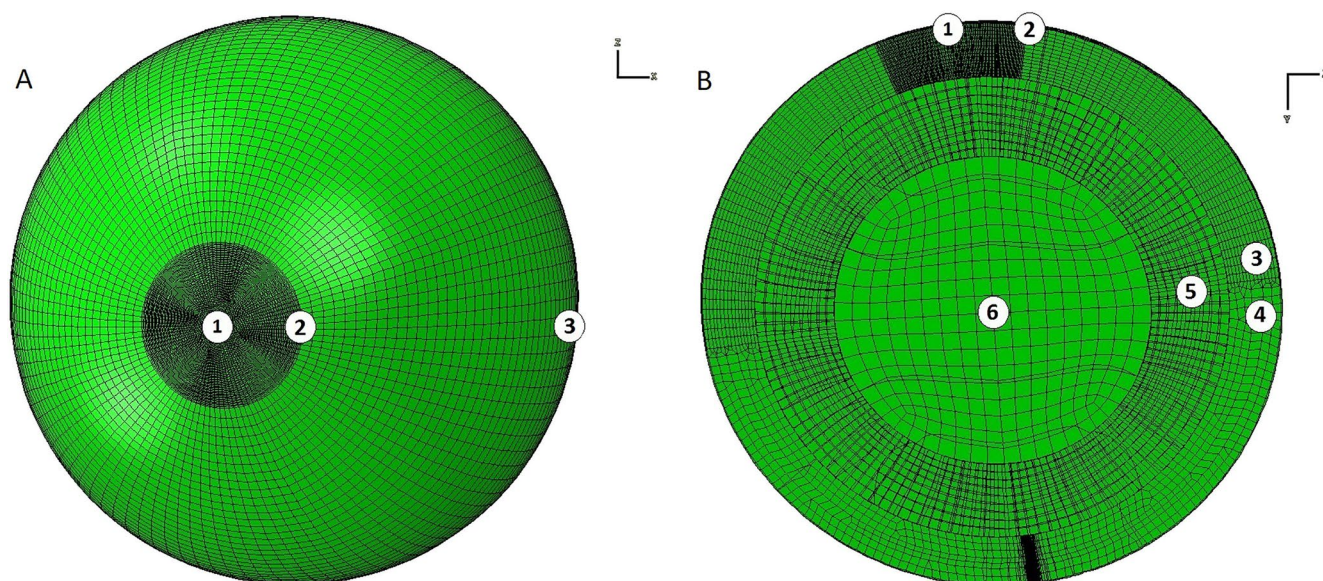
Figure 1. Finite element mesh (a: top down view left, b: cross section view) used for the 3D FE glacial isostatic adjustment (GIA) model. The high resolution area has a radius of 15° (from point 1 to point 2) and is centered at the Amundsen Sea Embayment (ASE; 108.3°W, 76°S). Element dimensions for all six designated regions can be found in in Table 1.

2. Method

2.1. 3D Finite Element Model

The 3D/3D-s model used in this study is a FE model based on the commercial software ABAQUS^{TM}, following the method of Wu (2004). In this approach a stress transformation is applied so that the equations of motion are transformed into a form in which they can be implemented in the FE model. Self-gravitation is applied by computing the change in gravitational potential and applying it to the model as a new force at each density interface after which a new deformation can be computed and the process is repeated until convergence. The FE model that formed the basis of the rotational dynamics model in Hu et al. (2017) has been modified to incorporate GIA, lateral varying viscosity, and variable resolution. A high resolution region (HRR) has been introduced to the model to simulate GIA in small regions, such as the ASE. A global model with high resolution is not computationally feasible. Therefore, the model was divided in sections with different element sizes, with the smallest elements located in the HRR around the ASE and larger elements located in the far-field (FF; Figure 1). For this study the HRR is centered around the ASE and its smallest elements surfaces are 25 by 25 km. The element size of the far-field for this study is based on similar models without a HRR and a focus on continent scale GIA (van der Wal et al., 2015) and measure 200 km by 200 km near the equator. All element sizes are given in Table 1. Furthermore, deeper layers such as the lower mantle are meshed with a lower resolution to further reduce the total amount of elements. Depending on the model the computation time of the model would be on the order of 5–10 days. A benchmark of the FE model in this configuration for different test cases can be found in the Supporting Information. The code has been benchmarked with results from Martinec et al. (2018) for a spherical cap load near the North pole (64°N 75°W). It can be seen in Figure 3 of the supplementary material that the deflection underneath and near ice masses differs between the FE model and the benchmark model by 1.3% for a resolution of ± 0.25° × 0.25°. This is a significant improvement from the 2° × 2° of earlier implementations of the method of Wu (2004), including the 0.5° × 0.5° spatial resolution from the recent study of Huang

Table 1

Approximate Size of Elements for Sections of the Model Shown in Figure 1, at the Top of the Specific Layer

Location	Latitudinal size [km]	Longitudinal size [km]	Radial size [km]
1. Center HRR	25	25	50
2. Rim HRR	27	92	50
3. FF south of equator	200	200	50
4. FF north of equator	200	200	200
5. Lower mantle	200	200	200
6. Core	400	400	400

FF, far-field; HRR, high resolution region.

Table 2
Earth Model Used for the 3D GIA Model

Layer	Depth top of layer (km)	Density (kg / m³)	Youngs Modulus (Pa)	Viscosity (Pa · s)
Top elastic layer	0	3,037	$0.506 \cdot 10^{11}$	∞
Upper mantle	30	3,438	$0.704 \cdot 10^{11}$	3D
Transition zone	420	3,871	$1.055 \cdot 10^{11}$	Case specific[a]
Lower mantle 1	670	4,978	$2.283 \cdot 10^{11}$	$2 \cdot 10^{21}$
Lower mantle 2	1,171	4,978	$2.283 \cdot 10^{11}$	$2 \cdot 10^{21}$
Core	2,911	10,750	0	0

GIA, glacial isostatic adjustment.

[a]Depends on the temperature and chosen rheology parameters.

et al. (2019). It must be noted that the resolution is lower when compared to the global finite volume models used in Powell et al. (2020), or local normal mode model, such as Barletta et al. (2018) whose grid points are approximately 5 km apart.

The sea-level equation (SLE) is included according to the algorithm from Kendall et al. (2005) including changes in shorelines due to melt-water influx and changing shorelines (Johnston, 1993; Milne & Mitrovica, 1998). Small changes to the algorithm of Kendall et al. (2005) are applied to make it suitable for the FEM; these can be found in the Supporting Information. The most important changes are that the 3D model can directly calculate the deflection through its FEM component of the code and the gravitational field changes by using (Wu, 2004), instead of having to solve for them. Furthermore, the 3D model uses the change in ice load instead of the total ice load, for which the algorithm has to be adopted. Additionally, some functionalities were added to decrease computation time. The effect of rotational feedback is small on the spatial scale that we consider and is not included. It is important to note that the sea-level equation can be solved at a higher resolution than the FE grid. This allows shoreline locations which experience large force changes over time as a result of ice grounding to be modeled with high spatial accuracy. Here, the SLE is solved in a global equiangular grid of 0.25° × 0.25°. It must be noted that the full Sea level equation (SLE) is only used for the modeling of the ASE with a full glacial cycle ice history, to investigate the effect of Pleistocene ice history on present-day uplift rate and stress-dependent viscosity. For all other simulations an eustatic sea level with static shorelines is used to make the results comparable with a local 1D model.

2.2. Rheology

We use a Maxwell rheology in which elastic and viscous (steady-state) deformation are summed. Elastic parameters for the Earth model are the same as the M3-L70-V01 model (Spada et al., 2011) see Table 2. The entire model is assumed incompressible ($\nu = 0.5$) as compressibility is not-trivial to add to the model (Wong & Wu, 2019). The 1D model discussed later is compressible. We have verified that differences introduced by the assumption of incompressibility are much smaller than the effect of rheology studied here (see Supporting Information S1). The top layer of the model is fully elastic and has a thickness of 30 km. This is the minimum thickness of the lithosphere in off-shore west Antarctica (Pappa et al., 2019). The lithosphere in most of Antarctica will be thicker, as the temperature results in higher effective viscosity and consequently larger effective thickness of the lithosphere. As a consequence the density of the top mantle layer has been adjusted to 3,438 kg/m³, to keep the total mass of the Earth constant. Below the top layer, the layers are viscoelastic and the effective viscosity determines whether there is significant viscous deformation over the timescale of the loading. Thus, the lithospheric thickness defined as the top part of the Earth that behaves fully elastic is defined implicitly by the effective viscosity. For the short time scales we consider in our study the lithospheric thickness will be effectively larger than for a study for the full

glacial cycle for the same Earth model (Nield et al., 2018). In the upper mantle, diffusion and dislocation creep parameters B are as calculated in Equation 3. The 3D variation in the creep parameters is determined by the temperature. Temperature estimates are discussed in the next section. For the transition zone the viscosity was calculated following the same procedure, however in this layer the temperature is uniform with depth and is extrapolated from the respective temperature models. Viscosity derived from shear wave velocities shows relatively high viscosity in the transition zone and smaller lateral variations (Ivins et al., 2021) which likely means little sensitivity to 3D viscosity in the transition zone for the small ice loads used here. And the load induced stresses are negligible compared to the upper mantle. Therefore, it was chosen to use linear rheology for these elements as it saves computation time without influencing the results.

We assume that the rheology of the upper mantle is controlled by olivine and uses the steady-state flow law (when no melt is assumed) compiled by Hirth and Kohlstedt (2003):

$$\dot{\epsilon} = A q^n d^{-p} f_{H_2O}^r e^{-\frac{E+PV}{RT}} \tag{1}$$

here, A and α are experimentally determined constants. Furthermore, q represents the stress present. The parameter d represents the grain size, while f_{H_2O} represents the water content within the olivine. Uncertainty in the the parameter d and f_{H_2O} will lead to much larger changes in viscosity than the uncertainty in activation enthalpy resulting from experiments and these will be used as free parameters that are varied between rheology models. Viscosity changes as a result of, for example, activation enthalpy are smaller. Pressure P is assumed to increase linearly with depth Z according to $P(\text{GPa}) = 0.0333 \cdot Z(\text{km})$ (Kearey et al., 2009). R is the gas constant and T the local temperature. Temperature and stress are the only parameters that can vary with location, with temperature variations having a larger control on viscosity. Finally E is the activation energy and V is the activation volume.

Deformation mechanisms for olivine under upper mantle conditions include diffusion creep, dislocation creep and grain boundary sliding (Hirth & Kohlstedt, 2015) which can be combined to obtained an upper mantle flow law (e.g. Ivins et al. (2021)). Here we use the two main mechanisms diffusion creep and dislocation creep which suffices for our goal of having a mix of linear and non-linear rheology. They can both be represented by Equation 1. Diffusion creep rate is strongly dependent on grain size, with grain size exponent p of 3, but only linearly dependent on stress (stress exponent n of 1) and water content (water content exponent r of 1). Dislocation creep rate is linearly dependent on grain size ($p = 1$) and non-linearly dependent on stress ($n > 2$) and water content ($r = 1.2$). The non-linear stress-dependence gives rise to the time-dependence of effective viscosity. The deformation mechanisms have different activation energy and volume, as given in Hirth and Kohlstedt (2003). Following van der Wal et al. (2010) the two mechanisms are combined in a so-called composite rheology.

The olivine rheology is implemented in the FE model as follows. It is postulated that the relation between the stress and strain rate measured in a uni-axial experiment as compiled in Hirth and Kohlstedt (2003) also holds for the relation between the equivalent stress and equivalent strain rate which are invariants of the stress and strain tensor respectively (Ranalli, 1995):

$$\dot{\tilde{\epsilon}} = B \tilde{q}^n \tag{2}$$

where B is derived from Equation 1

$$B = A d^{-p} f_{H_2O}^r e^{-\frac{E+PV}{RT}} \tag{3}$$

The equivalent stress used here is the so-called Von Mises stress:

$$\tilde{q} = \sqrt{\frac{3}{2} q_{ij} q_{ij}} \tag{4}$$

and the corresponding uni-axial equivalent strain rate is

$$\dot{\tilde{\epsilon}} = \sqrt{\frac{2}{3}\dot{\epsilon}_{ij}\dot{\epsilon}_{ij}}$$

(5)

To get a relation between tensor components, assume that the components of the deviatoric strain rate tensor are proportional to the components of the deviatoric stress tensor with a factor λ (Ranalli, 1995):

$$\dot{\epsilon}_{ij} = \lambda q_{ij}$$

(6)

it can then be derived (van der Wal et al., 2013) that:

$$\dot{\epsilon}_{ij} = \frac{3}{2}B\tilde{q}^{n-1}q_{ij}$$

(7)

in ABAQUS the uniaxial equivalent strain increments are computed from time increments Δt as follows:

$$\Delta\tilde{\epsilon} = B\tilde{q}^{n}\Delta t$$

(8)

and components of the incremental strain tensor are computed as:

$$\Delta\epsilon_{ij} = \Delta\tilde{\epsilon}\frac{\delta\tilde{q}}{\delta q_{ij}}$$

(9)

where the derivative is (Zhang, 2005):

$$\frac{\delta\tilde{q}}{\delta q_{ij}} = \frac{3q_{ij}}{2\tilde{q}}$$

(10)

combining Equations 8–10 yields:

$$\Delta\epsilon_{ij} = \frac{3}{2}B\tilde{q}^{n-1}q_{ij}\Delta t$$

(11)

which agrees with Equation 7. The stress transformation of Wu (2004) does not affect the deviatoric stress so the above equations can be used directly.

The equations in this section hold for both diffusion creep and dislocation creep. In order to implement the composite rheology we use the fact that diffusion creep and dislocation creep occur simultaneously and their components can be added for the uni-axial flow law and for the relation between the uni-axial equivalent strain rate and the Von Mises stress that is input in ABAQUS (Equation 8):

$$\Delta\epsilon_{ij} = \frac{3}{2}(B_{diff} + B_{disl}\tilde{q}^{n-1})q_{ij}\Delta t$$

(12)

$$\dot{\tilde{\epsilon}} = \frac{3}{2}(B_{diff}\tilde{q} + B_{disl}\tilde{q}^{n})\Delta t$$

(13)

defining an effective viscosity η_{eff} as $\eta_{eff} = \frac{\tilde{q}}{2\dot{\tilde{\epsilon}}}$, it follows from Equation 13 that (van der Wal et al., 2013)

$$\eta_{eff} = \frac{1}{3B_{diff} + 3B_{disl}\tilde{q}^{n-1}}$$

(14)

The viscosity depends directly on temperature estimates, and can vary strongly as a function of grain size and water content (Barnhoorn et al., 2011). This is in contrast to an approach whereby seismic velocity anomalies are scaled to viscosity anomalies (as e.g., done in Gomez et al., 2018; Hay et al., 2017; Powell et al., 2020). In that approach a background viscosity is needed, which can be informed by parameters from GIA or other geodynamic studies. Our approach does not require a background viscosity model and can provide viscosity values that are independent from parameters in geodynamic studies. However, they depend strongly on grain size and water content which are unknown, and hence some guidance on these from other studies are necessary. In principal grain size and water content can also be varied with location but as we have little information on the grain size and water content across Antarctica (van der Wal et al., 2015) they are kept spatially homogeneous. We have chosen the values based on a fit with GPS uplift values, as
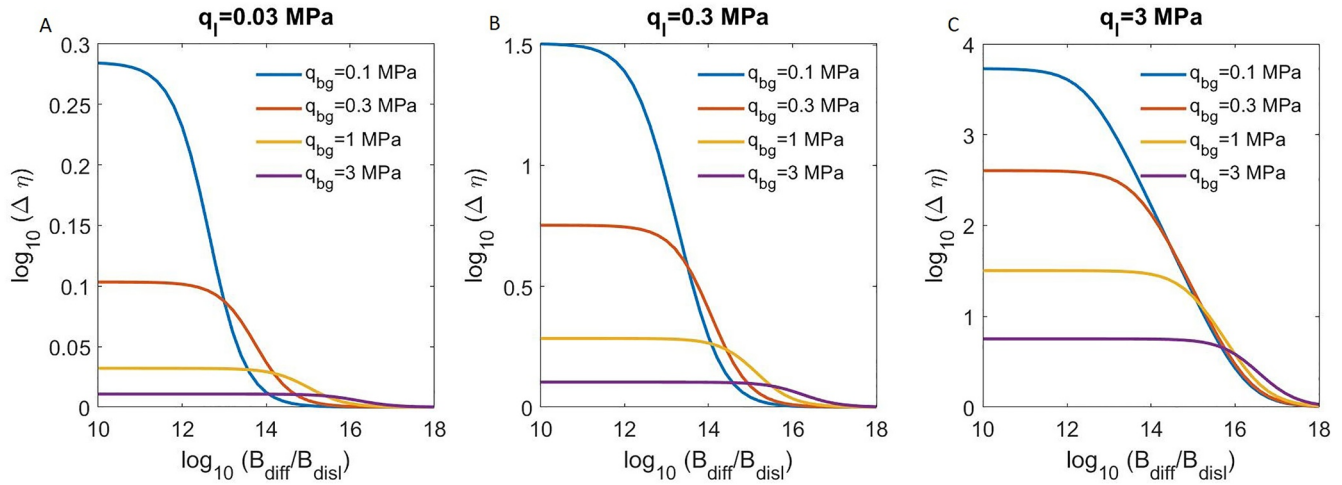
Figure 2. Decrease in viscosity $\log_{10}(\Delta\eta)$ as a function of different non-linear rheology settings B_{diff}/B_{disl} with different values of background stress q_{bg} present. (a) Drop in viscosity for different background stresses as a consequence of 30 kPa of load induced stress ($q_l = 0.03$ MPa), which is comparable to the stress in the upper mantle at about 200–400 from the main Amundsen Sea Embayment (ASE) load. (b) Drop in viscosity for different background stresses as a consequence of 0.3 MPa of load induced stress ($q_l = 0.3$ MPa), which is comparable to stress in the upper mantle directly underneath the recently diminished ASE glaciers. (c) Drop in viscosity for different background stresses as a consequence of 3 MPa of load induced stress ($q_l = 3$ MPa), which is comparable to the stress from ice sheets of several kilometers thick as present during the LGM.

will be explained in the results section. For the areas outside of Antarctica we no longer compute dislocation creep and diffusion creep parameters from temperature, water content and grain size (Equation 3), but we set them to predefined values of $1.11\cdot10^{-22}\,\mathrm{Pa^{-1}s^{-1}}$ and the dislocation parameter to be $3.33\cdot10^{-35}\,\mathrm{Pa^{-3.5}s^{-1}}$, with $n = 3.5$, which gives a good fit with global RSL data (van der Wal et al., 2010). This will effectively simulate a viscosity of $3.0\cdot10^{21}\,\mathrm{Pa\cdot s}$ when no stress is considered. The composite rheology changes to a Maxwell rheology below 420 km depth for two reasons. First of the temperature models used did not contain spatial variation anymore at this depth and second stress at this depth turned out to be negligible for the considered load in the ASE, thus voiding the need for the more computationally heavy composite rheology type elements. For the deeper mantle (>670 km) we considered a linear Maxwell rheology with a viscosity of $2\cdot10^{21}\,\mathrm{Pa\cdot s}$.

Equation 14 shows that the effective viscosity always decreases with an increased Von Mises stress. The affect of adding a predefined Von Mises stress in a non-linear rheology was investigated by Wu (2001) and for composite rheology by Gasperini et al. (1992). The main conclusion from these studies is that realistic predefined mantle stresses can significantly affect the GIA process, depending on their magnitude, as they impact the stress invariant and thus the effective viscosity below the load over time.

In our composite rheology, the change in viscosity due to a load induced stress q_l in the presence of a background stress q_{bg} can be defined as follows:

$$\Delta\eta_{q_{bg}} = \frac{1}{3B_{diff} + 3B_{disl}q_{bg}^{n-1}} - \frac{1}{3B_{diff} + 3B_{disl}(q_{bg} + q_l)^{n-1}} \tag{15}$$

this equation depends on the importance of dislocation creep with respect to diffusion creep, and hence on the value of $\dfrac{B_{diff}}{B_{disl}}$ as well as the load induced stress. If we plot the results of Equation 15 for different values of q_l we can see the aforementioned drop in effective viscosity in the presence of background stress as a function of $\dfrac{B_{diff}}{B_{disl}}$, see Figure 2. We see that for rheologies where the contribution of dislocation creep is large ($\log_{10}(B_{diff}/B_{disl}) = 10$), a large background stress will decrease the drop in viscosity as a consequence of the load induced stress. In these cases the viscosity is already lowered significantly by the background stress itself, so the extra stress from the load has little impact. If on the other hand dislocation creep has a small contribution, the drop in viscosity caused by load induced stresses will always be low, regardless of background

stress. In between the extreme cases there exists a window (around $\log_{10}(B_{diff}/B_{disl}) \approx 13.5 - 18$ depending on the load magnitude) where larger background stresses will also lead to larger drops in viscosity when a load is applied. This window is relevant as it exists in the range of plausible rheologies. This means that, while the general rule is that the presence of background stress reduces the decrease in viscosity for a given load, in specific situations the presence of a background stress can also strengthen the effect of load induced stress and thus time dependency for the solid earth response.

In reality the situation is more complicated because the Von Mises stress can both increase and decrease if a background stress field is added, depending on the magnitude and direction of the individual stress components (Schmeling, 1987). In Section 3.5, we investigate the effect of stresses induced by loads from the last glacial cycle on the GIA response due to recent ice loading. Both loading processes are simulated in the model, hence the stress addition takes place inside the FE model. This is the first time that the stress interaction from long timescale GIA and short timescale GIA are investigated. While we did not investigate the influence of tectonic stress, there is tectonic movement in and around West Antarctica (Eagles, Gohl, & Larter, 2009; Eagles, Larter, et al., 2009) that can also form an important source for background stress. This means tectonics background stress can have similar interactions with the short time scale ice load induced as the LGM induced stress and would be worth investigating in future research.

2.3. Temperature Models of the Upper Mantle

For this study two new temperature models are used. Both models are created using different variants of the LitMod3D modeling framework (Fullea et al., 2009, 2018), which will be described further below. As a key characteristic, LitMod3D links thermochemical conditions in the Earth to geophysical-petrological observations. The rock composition is defined using the major oxide system CFMAS (CaO, FeO, MgO, Al_2O_3, and SiO_2). These oxides represent 98% of the mantle material (McDonough & Sun, 1995) and form five independent variables, which are combined in the four main mantle mineral phases (olivine, pyroxene, plagioclase, and spinel). Stable mineral assemblages are determined using Gibbs free energy minimization. The lithosphere-asthenosphere boundary is defined by the 1,315°C geotherm. Heat transfer in the lithosphere is assumed to be by heat conduction; below the lithosphere the temperature follows the mantle adiabat with a potential temperature of 1,345°C (Fullea et al., 2009). There conduction and convection can both occur, while between 1,400°C and 1,500°C convection is assumed to dominate. For a certain composition, LitMod3D computes the density and elastic modulus. Different observations can be used to constrain the composition, with the most important being topography and gravity data as explained in the following.

The first temperature estimate used in this study was developed by Pappa et al. (2019) by combining data from topography, seismology and satellite gravity in a lithospheric model of Antarctica in the framework of ESA-project GOCE+. The resulting temperature model for the lithosphere and sub-lithospheric upper mantle is referred to as the GOCE + model in the following. The authors used LitMod3D (Afonso et al., 2008; Fullea et al., 2009), which is an older variant of the LitMod3D software and provides a forward modeling framework in a finite difference discretization. Prior definitions in terms of crustal and mantle domains have been made in the GOCE + model. The Moho is defined by a density contrast of 400 kg m^{-3}. The crust of the GOCE + model is divided in a continental and an ocean domain. The continental crust is vertically divided into three layers, representing upper, middle, and lower crust. According to the geological provinces of Antarctica and their estimated tectonothermal age, domains of the lithospheric mantle are defined and described by different peridotitic rock compositions. Using seismologically derived models of the Moho (An et al., 2015a) and the lithosphere-asthenosphere boundary (LAB; An et al., 2015b) as a starting model, Pappa et al. (2019) modified the Moho and LAB depths in order to achieve a fit of isostasy (topography) and gravity gradients in contrast to models that are purely constrained on their seismological data. Instead, independent seismically derived Moho depth estimates from various other studies are used as a *a posteriori* benchmark to evaluate the modeled crustal thickness. As a result, the GOCE + model simultaneously fits isostatic topography, satellite gravity gradients, and seismic Moho depth estimates to a large extent. Because LitMod3D uses adiabatic temperature gradients, dynamic topography is not included within this model. As mentioned above, mantle rock compositions are predefined in this model based on geological studies on the tectonothermal age. Since the rock densities inside this model are modeled in a thermodynamically and internally consistent way, a 3D temperature field of the Antarctic lithosphere results. The temperature
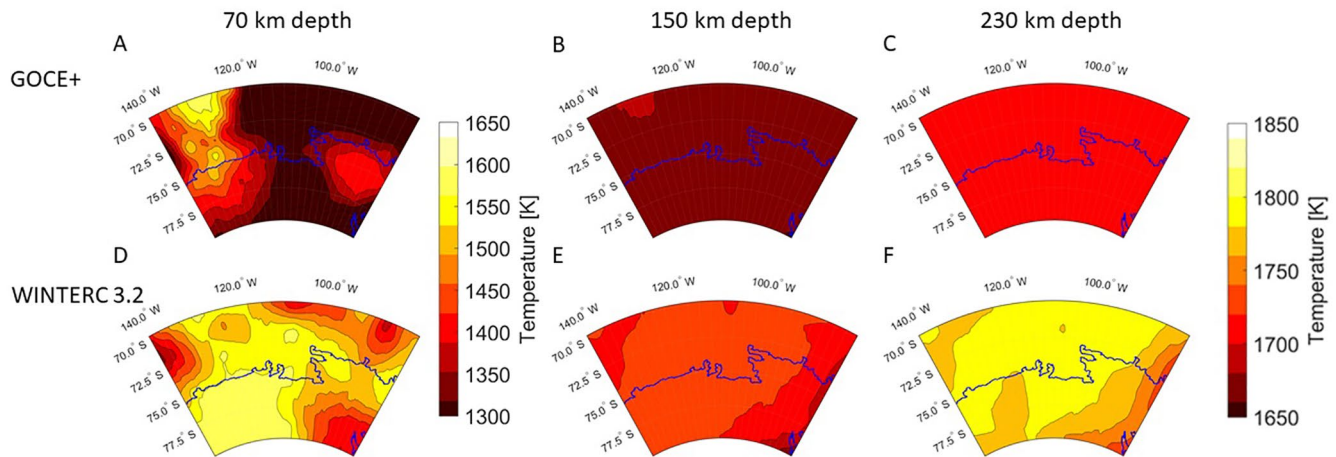
Figure 3. Temperature at 70, 150, and 230 km depth for the GOCE + model (top a–c) and WINTERC 3.2 model (bottom d–f) for the Amundsen Sea Embayment (ASE) and surrounding regions.

distribution of the GOCE + model for the ASE can be seen in the top row of Figures 3a–3c. Compared to the seismically derived temperature distribution of An et al. (2015b), temperatures are generally lower. This could be a result of the direct conversion of S-wave velocities into mantle temperatures in the model from An et al. (2015b), which does not consider the potential existence of melt or fluid inclusions and can thus be seen as an upper bound (An et al., 2015b).

The second temperature model is the WINTERC 3.2 model (Fullea et al., 2018). A newer version of Lit-Mod3D is used here, coming along with an inversion approach where a variety of geophysical parameters are simultaneously fit to many seismic, gravitational and heat flow observations. Isostasy is applied, as well as heat flow data, topography, and surface-wave dispersion curves analysis (Schaeffer & Lebedev, 2013) as input. The fit is performed by changing the composition (notably the aluminum content of the lithosphere), the temperature and pressure within the lithosphere model. While changing mantle composition to simultaneously fit multiple data sets in itself is a selling point for the robustness of the model. The process has its shortcomings such as the fact that converting seismic velocity to gravity through linearized scaling factors ignores known petrological non-linear effects. These non-linear petrological effects are accounted for when calculating density and seismic velocities within a thermodynamical self-consistent framework. It should be noted that in this approach the Moho depth is predefined and, in contrast to the GOCE + model, mantle rock composition is allowed to vary. By estimating the residual isostatic topography resulting from density variations, a proxy to dynamic topography is incorporated in the model. The WINTERC 3.2 model shows good agreement with temperature patterns of seismological models. Temperature maps for the ASE and surrounding regions can be seen in the bottom row of Figures 3d–3f.

It can be seen that the GOCE + model is colder than WINTERC 3.2 model. This is in agreement with the comparison between An et al. (2015b) and the GOCE + temperature estimates in Pappa et al. (2019). This will result in the GOCE + model having a higher viscosity than the WINTERC 3.2 model with the same rheology parameters, making it less responsive to short term ice loads. We also see local differences in the spatial pattern between both models. At 70 km a colder region is realized in the GOCE + model, with warmer parts in the top part of the mantle to the east and west of the ASE. In the deeper layers of the GOCE + model there is still a colder area north of the coast (110W°) but it is much less pronounced. In contrast, the WINTERC 3.2 model is less uniform in the top layer and has a warmer mantle underneath the ASE, near the northern coast and to the west of the ASE. This translates to a thinner elastic lithosphere in these locations. In the deeper layers of the WINTERC 3.2 model temperatures are more uniform. The most important deviations from a uniform distribution are a slightly colder area to the west of the ASE aswell as a colder area in eastern direction toward the Antarctic Peninsula. Seismic studies, for example Shen et al. (2020), predict low seismic velocities and thus high temperature directly beneath the glaciers of the ASE, showing similarities with the WINTERC 3.2 model.
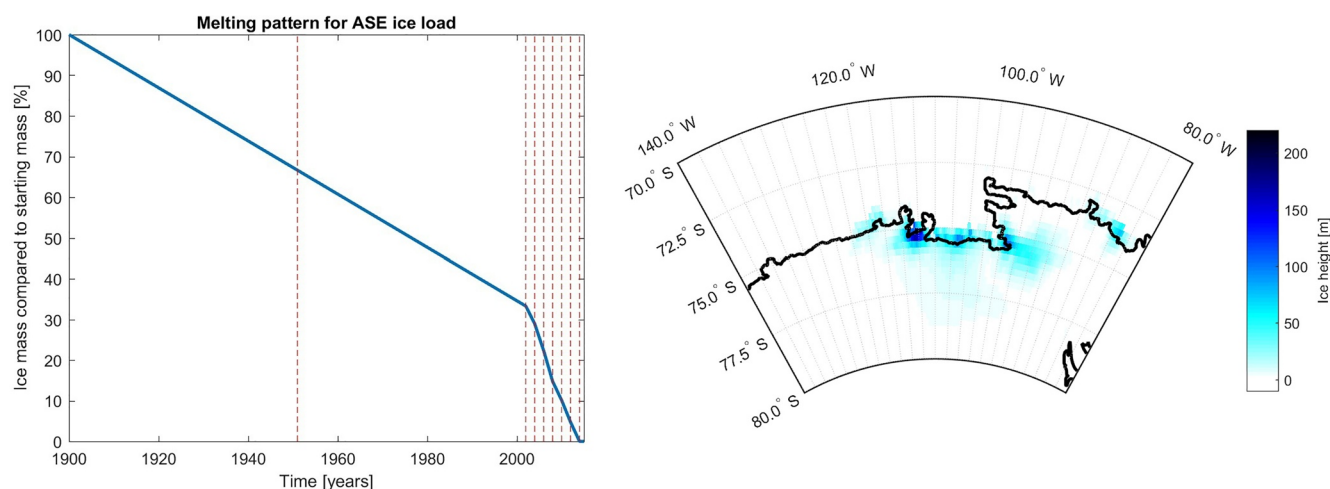
Figure 4. Ice model with the total mass change through time on the left and the spatial distribution on the right. The dashed red lines indicate the initial time steps at which the ice load is defined.

It is important to note that while there is focus on the ASE itself we use these models to construct a lateral heterogeneous viscosity map for the entire continent of Antarctica. This is done because uplift can be sensitive to viscosity in a large area, and because the simulation of the last glacial cycle was done for the entire continent.

2.4. Ice History Model

The ice history is derived from the one proposed for the ASE in Barletta et al. (2018). In there, high resolution present-day ice changes during the time period 2002–2014 are extrapolated backwards in time until 1900 (Figure 4). The extrapolated ice loss trend is an overestimation of the actual trend as ice change measurements since the 1970's conclude that ice loss has been speeding up in recent years (Gardner et al., 2018; Mouginot et al., 2014). In Barletta et al. (2018) a grid search for the rheology settings for multiple ice history scenarios is performed to find the best fit to the observed GPS uplift. It is found that the ice history scenario which uses 25% of the current trend for the period between 1900 and 2002, yields the best fit. We have also assumed that the rate of ice mass loss in the first half of the twentieth century is equal to that of the period of 1950–1970, which is also debatable (Ivins et al., 2002). At the start of the simulation it is assumed that the load present in 1900 has been present for 30 ky which is practically equivalent to assuming isostatic equilibrium, which is achieved. In Powell et al. (2020) no loading is applied prior to recent satellite measured increased ice mass loss (1992). It must be noted that in our setup we initially assume no background stresses from prior ice loading,, which were almost certainly present due to increased ice mass loss after 1850 (Little Ice Age; Ivins et al., 2000). The influence of background stress on the present day uplift cannot be assumed to be negligible and will be treated in Section 3.5. The effect of pre-1900 ice loads on current uplift rates is assumed to be small. Furthermore, the ice load from Barletta et al. (2018) was tailored to fit the 1D model specifically, so it could be inconsistent with the 3D and 3D-s models introduced here, However, in this study we perform sensitivity studies comparing the different rheologies. Uncertainties in the ice history are not expected to significantly influence the characteristic differences in model behavior. Model sensitivity runs with more and slightly altered starting ice showed different uplift rates but the same characteristic difference between models. Because the ice history and the local GIA model used in Barletta et al. (2018) are of a higher resolution than the global FE model used in this study, the ice history is down-sampled from ±1 km to the size of the FE elements discussed in the method section. This down-sampling is also done for the 1D model input to eliminate possible differences as a consequence of different spatial resolution. The ice load that is used as input for the model can be seen in Figure 4.

Table 3
GIA Associated Vertical Uplift (Barletta et al., 2018; Liu et al., 2018) of GPS Stations in or Near the Amundsen Sea Embayment (ASE)

Stations	Uplift [mm/y]	T_{obs} [y]
BACK	10.07 ± 1.5	8.036
BERP	19.12 ± 0.7	10.386
INMN	26.05 ± 2.4	1.252
LPLY	3.93 ± 0.5	8.241
THUR	−3.99 ± 0.8	8.236
TOMO	29.90 ± 3.0	2.203
SDLY	−3.83 ± 1.04	5.0

GIA, glacial isostatic adjustment.

2.5. The 1D Normal Mode Model

To evaluate the effect of 3D viscosity, the 3D model output is assumed to represent predictions for a more realistic Earth. Therefore, we seek 1D models that produce predictions compatible with those of the more granular view of the Earth's real structure. Here we use the viscoelastic uplift component for a 1D compressible Maxwell Earth model, in response to the ice-mass loss, as in Barletta et al. (2018). The model is based on the normal mode viscoelastic theory where we use the VE-CL0V3RS v3.6 model (Barletta et al., 2018) to compute the elementary viscoelastic time dependent Green's functions (convolved with Heaviside function) up to degree 1,500, and assume that at higher degrees they do not change with time as they sample elastic response only so the combined Green's function is negligible. The structure of the elastic parameter is PREM-based (Dziewonski & Anderson, 1981) with 31 layers, while the viscous parameters are divided into five parts. The first layer is the elastic lithosphere, which is varied in thickness from 40 to 70 km and represents the crust and the part of the lithosphere that behaves elastically on the timescale of loading. 40 km was used as a minimum here, because in Barletta et al. (2018) all values of 40 km showed a worse fit than those for a thicker elastic lithosphere and thin lithosphere was only observed off-shore West Antarctica (Pappa et al., 2019). The second layer is the shallow upper mantle (SUM), which is defined from the bottom of the elastic layer to a depth of 200 km. The third layer is the deeper upper mantle (DUM), which is defined from 200 to 400 km depth. Viscosities in the SUM and DUM will be varied to achieve a good fit with respect to the uplift from the 3D and 3D-s models. The final two layers are the transition zone and the lower mantle, which are defined from 400 to 670 km and 670 to 2,891 km (core-mantle boundary), respectively. These layers have a viscosity of 10^{21} Pa · s in this study. In the Supporting Information, we have tested this 1D setup versus the 3D setup. The maximum difference found was 1.15 mm/y and the average difference was 0.24 m/y, which as we will later see, are not consequential for the results.

2.6. GPS Data

For the GPS stations we have selected the same 6 GPS stations as were used in Barletta et al. (2018) with the addition of the SDLY station (Liu et al., 2018). The SDLY station is located at 125.9746°W, 77.1353°S in Marie Byrd Land, adjacent to the ASE sector. It was included to also have information on the western side of the ASE. The GPS uplift rates have been corrected with modeled elastic uplift. The elastically corrected GPS uplift, their standard deviation and length of the time-series, T_{obs}, can be seen in Table 3.

Table 4

χ_{cr}^2 Test Statistics per Model Setting

Grain size [mm]	Water content [H_2O ppm]	GOCE + model χ_{cr}^2	WINTERC model χ_{cr}^2
8	1,000	62.4	30.3
6	1,000	25.9	222.6
4	1,000	10.7	710.8
4	500	10.2	231.8
4	0	109.8	–

2.7. Statistical Model Comparison

In order to compare all models evaluated in this study we use a χ^2-test with the χ_{cr}^2 statistic that is also used in Barletta et al. (2018):

$$\chi_{cr}^2 = \frac{1}{N_{GPS} - 1} \sum_{i=1}^{N_{GPS}} \left(\frac{M_i - m_i}{SD_{av}} \right)^2 \tag{16}$$

where, M_i is the uplift at the ith-station of the reference model, while m_i represents the 1D model uplift at the same station. Because both 1D models and 3D models provide exact results and thus no error estimate, we have assumed the standard deviation SD_{av} as the average standard deviation (1.42 mm/y) of all the real GPS-stations (see Section 2.6). We use the average instead of the individual standard deviation to avoid introducing a weighting bias to the stations. While the magnitude of this value might be debated, it does not change the ranking of the goodness of fit for models with respect to each other.

To determine whether or not models significantly differ from one another we used a chi-square goodness of fit test,

$$\alpha < \int_{\chi_{cr}^2}^{\infty} \chi^2(k) \tag{17}$$

where, k is the degrees of freedom for the model. In the standard case of the ASE with 7 GPS stations (as seen in Section 2.6) and a significance level α of 0.05% this would mean that if $\chi_{cr}^2 > 9.49$ the null-hypotheses is rejected and the model is deemed significantly different from the (synthetic or real) measurements.

We will compare the 1D model results to 3D/3D-s models by first selecting rheology parameters for the 3D/3D-s models. We find those rheology parameters by fitting a set of rheology parameters combined with both the GOCE+ and WINTERC 3.2 temperature distribution to GPS data from the ASE region. The uplift of this best fitting model will be considered as the model standard that 1D models can then evaluate. Then, we investigate how well a best fitting 1D model will approximate the average 3D/3D-s viscosity. After this, we will investigate whether 3D viscosity results in significantly different uplift rates. Additionally we will inquire if the results are affected by the placement of GPS stations, thus making an assessment of the robustness of any previous findings. After this, we will investigate the effect of 3D-s modeled viscosity, by comparing 3D models to a 3D-s model. Finally, we will test whether including background stress will impact our previous results significantly.

3. Results

3.1. Rheology Parameter Selection Based on GPS Measurements

To determine which rheology settings would fit the ASE case, we used five sets of grain sizes and water content for the GOCE + model and four for the WINTERC 3.2 model. The number of models we can test is limited by the computational resources required. Therefore we performed a limited grid search of the best model by varying the grain size and water content. Grain size is varied from 4 to 8 mm, close to values that give a reasonable fit to uplift in the northern hemisphere (van der Wal et al., 2013). Water content is varied from fully dry to fully wet (1,000 ppm water content). Smaller grain size and larger water content both act to decrease viscosity. For both models we have chosen the rheologic parameters for which the chi-square between the model results and the GPS data was minimal.

Using Equation 16 we can compute the χ_{cr}^2 statistic for every model we considered. The results are shown in Table 4.

Based on the results in Table 4, we selected two models to focus on in this study, with a third model based on one of these first two models. The first model uses the GOCE + temperature with a grain size of 4 mm, a water content of 500 ppm and has a transition zone viscosity of 19.3 $\log_{10}(\text{Pa} \cdot \text{s})$, which will be referred to as

G405. The second model uses the WINTERC 3.2 temperature model with a grain size of 8 mm and a water content of 1,000 ppm and a transition zone viscosity of 19.7 $\log_{10}(Pa \cdot s)$, hence-forth referred to as W810. Two temperature models are used to differentiate between temperature model effects and general effects. Finally, a third model is used, which has the W810 settings for the rheology but dislocation creep is ignored by forcing the Von Mises stress to 0 using Equation 12. This is done in order to eliminate the non-linear component of the viscosity. Using a Von Mises stress of 0 will lead to an overestimation of viscosity. However, it is impossible to find a single accurate representative average Von Mises stress. The resulting model is a 3D model instead of a 3D-s model and will be referred to as W810-3D.

3.2. 1D Versus 3D/3D-s Models Viscosity

In Figure 5, the effective local viscosity is shown for G405 and W810 at two different points in time, approximately halfway through the deglaciation, in 1951, and at the end of the simulation in 2014. W810-3D is time-invariant and is shown in the bottom row. The viscosity highly correlates with the temperature map (Figure 3) for all models, with the only deviation present in high stress areas, which can be seen in Figure 6, near the ice load. The G405 model shows high values for the viscosity at 70 km depth with the exception of the western-most region. As the depth increases, the viscosity drops and becomes relatively uniform in horizontal directions. Changes in modeled effective viscosity over time are small for G405. This is despite the high stresses, with a maximum of 170 kPa in 1951 and 500 kPa in 2014. Due to lower water content and thus relatively small dislocation creep contribution, these high stress do not decrease viscosity to meaningful degrees.

For W810, at 70 km, there is a significant difference between the viscosities in the east and west of the ASE. In the center of the ASE, there is an area of very low viscosity ($10^{18.0}$ Pa · s) at 2014; this is where the glaciers are located with the largest mass discharge (Thwaites). This local low viscosity area is caused by the stress which is induced by the change in ice load. As the simulation approaches present day, the changes in ice load are larger than a few decades earlier. This increases the maximum stress from around 90 KPa in 1951 to approximately 175 kPa in 2014 for the final time step. The high local stresses cause dislocation creep to become a more dominant creep mechanism over a larger area which lowers the local viscosity over this area significantly. The load induced stress is reduced with increasing depth and therefore the change in effective viscosity over time is larger at 150 km than at 230 km. The last model, W810-3D, has the same east-west viscosity differences in the top part of the mantle as we observed in the W810 model. In both the W810 and the W810-3D model there is an area in the east of the ASE (95°W) that has a higher viscosity compared to the neighboring coastal regions. The deeper parts of the mantle are more uniform with slightly higher viscosities toward the east in the direction of the Antarctic rift system.

To see how well the best-fitting 1D model represents the 3D structure, a representative 1D viscosity and elastic thickness of the 3D and 3D-s models has to be determined. It is not obvious how such an average should be computed from a 3D/3D-s model with a local load. The first step in order to calculate the elastic lithosphere and the average effective viscosity is determining which elements behave viscoelastic and which elements are almost exclusively elastic. Although the thickness of the purely elastic layer is 30 km in the 3D-s model the effective elastic lithosphere thickness can be larger. The idea that elastic lithosphere thickness depends on loading duration or frequency depending has been adopted by others as well (Lau et al., 2020). In order to estimate the viscosity for which we would consider an element elastic we consider the relation between Maxwell viscosity and relaxation time:

$$\eta = \tau G \tag{18}$$

as a threshold for an elastic element, 3 times a relaxation time of a 150 years of simulation is assumed. With the shear modulus G as stated in Section 2. We find a threshold value of $10^{21.0}$ Pa · s. By assuming elements of a viscosity larger than $10^{21.0}$ Pa · s to be elastic we can derive an average elastic lithosphere thickness D_{litho} using relevant elements for GIA. The relevant elements are selected based on a threshold Von Mises stress, relative to the highest Von Mises stress at the depth at which the element is located in order to select elements the GIA in the ASE is actually sensitive to. For the elastic elements we did only consider elements in element layers (n_{layers}) in the elastic top layer or the SUM. We compute the fraction of elements within a
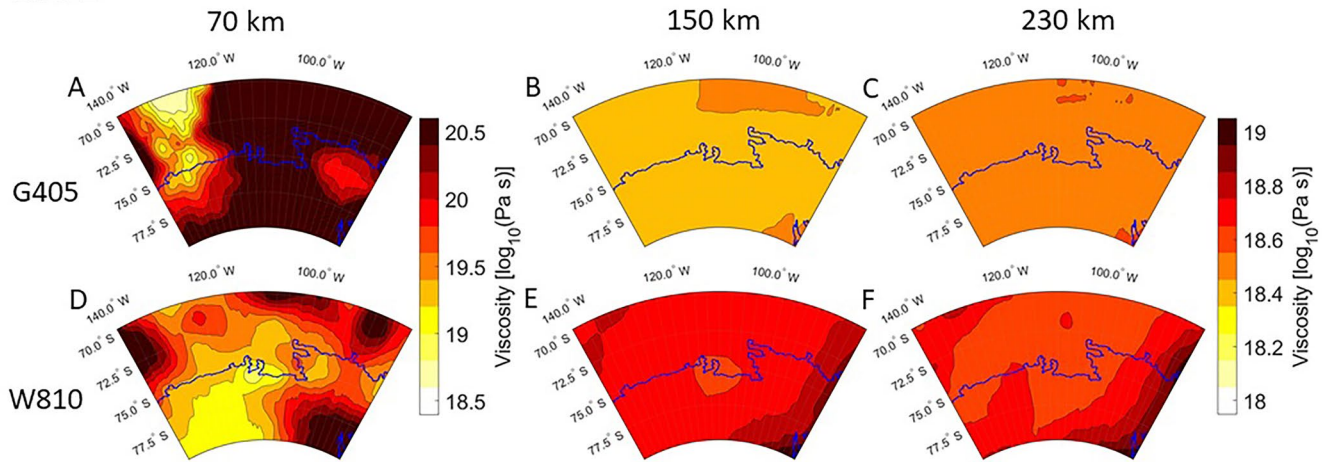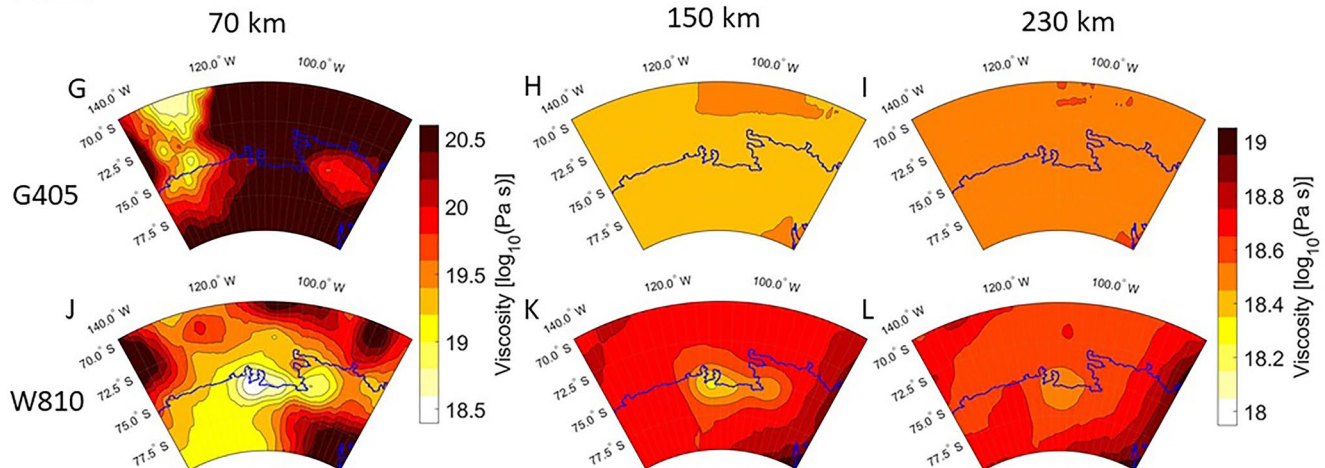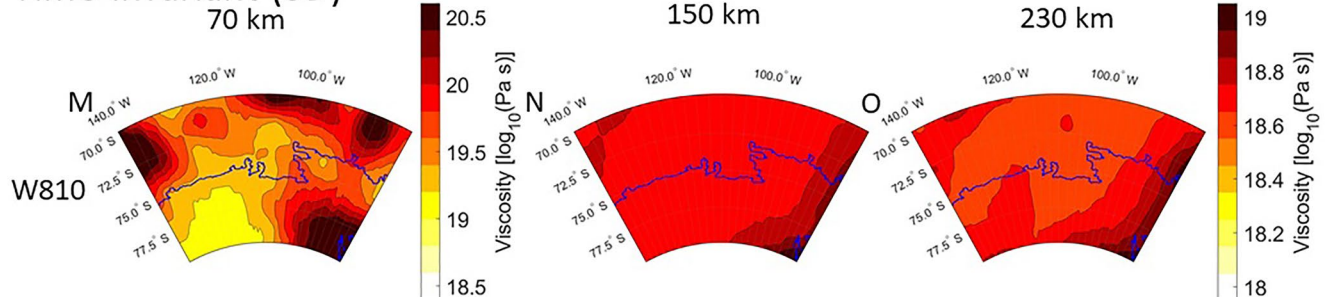
Figure 5. Viscosity of the Amundsen Sea Embayment (ASE) for three different depths: 70, 150, and 230 km. The models displayed are G405, W810 and W810-3D. The top two rows show the viscosity in 1951, which is near the halfway point of the simulation. Rows 3 and 4 shows viscosities in 2014, which is the last epoch in the simulation. The bottom row shows the viscosities for the W810 version with stress independent rheology.
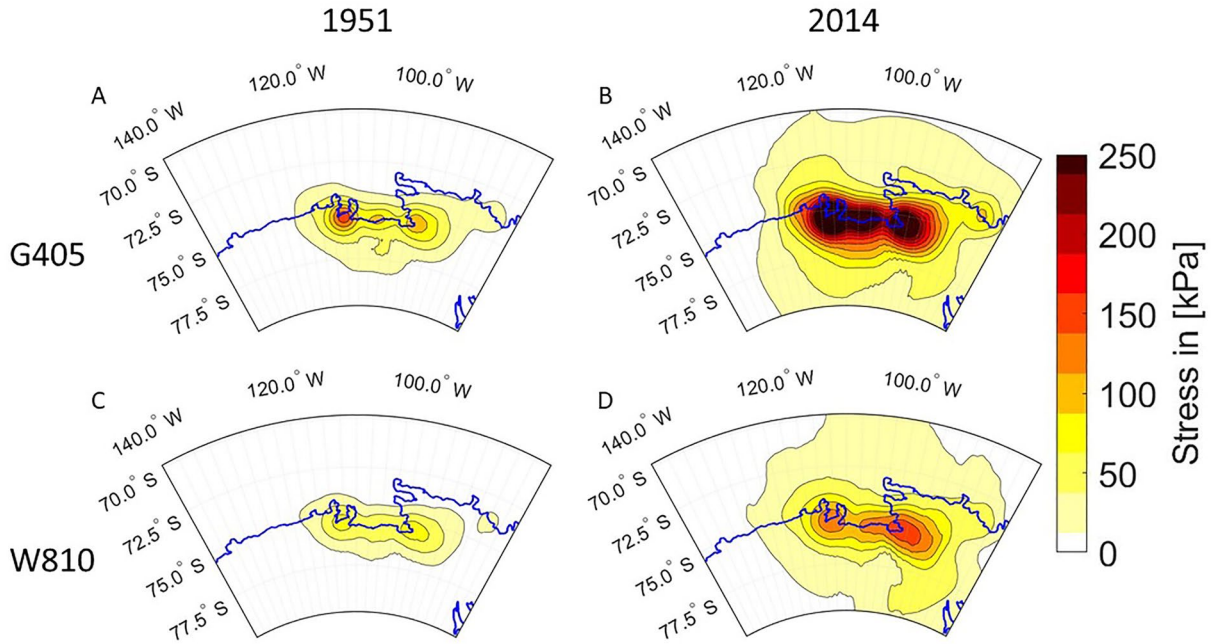
Figure 6. Von Mises stress in the upper mantle (70 km) of the Amundsen Sea Embayment (ASE). The models displayed are G405 (a and b) and W810 (c and d). The left column (a and c) shows the Von Mises Stress in 1951, which is near the halfway point of the simulation. The right column (b and d) displays the stress in 2014, which is the last epoch in the simulation.

selection that have a viscosity higher than $10^{21.0}$ Pa $\cdot$ s, $\dfrac{N_{\eta>21_i}}{N_{total_i}}$, and multiply this with the layer thickness D_i. Finally, the thickness of purely elastic layer, D_{crust} is added (Equation 19) and the results are shown in Table 5. We can see in Table 5 that G405 has a larger elastic lithosphere (53 km), while the elastic lithosphere thickness for the W810 and the W810-3D model is consistently 30 km.

$$D_{litho} = D_{crust} + \sum_{i=1}^{n_{layers}} D_i \frac{N_{\eta>21_i}}{N_{total_i}} \tag{19}$$

When we have defined which elements can be considered elastic we exclude them from the viscosity averaging computations. The average viscosity for the SUM and DUM is estimated by selecting the contributing elements based on a threshold Von Mises stress, relative to the highest Von Mises stress at the depth at which an element is located. An unweighted average is taken for the selected elements in this method. An overview of the method can be seen in Figure 7. Using this method, it can be investigated whether the best fit 1D model viscosities are close to the average viscosity values of the FE model (Table 5).

To benchmark how reliable the comparison is between the 1D and 3D/3D-s viscosity, a homogeneous 3D-s model was run with a top elastic layer of 40 km and non-linear rheology parameters that should correspond to an effective viscosity of 19.0 $\log_{10}$(Pa $\cdot$ s) for both the SUM and DUM. The best fit 1D model for this case was a model with a 40 km effective elastic lithosphere, a η_{SUM} of 18.8 $\log_{10}$(Pa $\cdot$ s) and a η_{DUM} of 19.0 $\log_{10}$ (Pa $\cdot$ s). While very close to the parameters of the 3D-s model, small differences between 1D and 3D/3D-s are introduced because of difference in discretization.

In Figure 8, it can be observed that there are multiple models with a good fit. The best fit 1D models in this paper for model G405 and W810-3D have a better fit to these 3D/3D-s models than to the GPS uplift rates, as was computed in Barletta et al. (2018) while model W810 has a similar value. Taking into account that for this experiment the ice history knows no discrepancy between the model standard and the 1D models approximating this, it can be concluded that G405 and W810-3D will be indistinguishable from a 1D model given the worse fit of any model to the uplift using 7 stations in reality. In order to distinguish between

Table 5
Top Section: Average Elastic Thickness (D_{litho}) and Viscosity for the Shallow Upper Mantle Layer (η_{SUM}) and the Deeper Upper Mantle Layer (η_{DUM}) of the 3D and 3D-s Models Using Stress Based Selection of the Elements

3D/3D-s model	Layer parameter	Time [AD]	G405	W810	W810-3D
Averaged Values of contributing elements	D_{litho} [km]	1951	59.8	30.0	30.0
		2014	53.2	30.0	30.0
	η_{SUM} [$\log_{10}(\mathrm{Pa}\cdot\mathrm{s})$]	1951	18.94	19.22	19.08
		2014	18.91	19.02	19.08
	η_{DUM} [$\log_{10}(\mathrm{Pa}\cdot\mathrm{s})$]	2014	18.66	18.88	18.89
Best fitting 1D models					
$N = 7$	D_{litho} [km]		70	40	50
	η_{SUM} [$\log_{10}(\mathrm{Pa}\cdot\mathrm{s})$]		19.2	18.4	19.0
	η_{DUM} [$\log_{10}(\mathrm{Pa}\cdot\mathrm{s})$]		18.4	18.8	18.8
$N = 1{,}440$	D_{litho} [km]		70	40	60
	η_{SUM} [$\log_{10}(\mathrm{Pa}\cdot\mathrm{s})$]		19.2	18.6	19.0
	η_{DUM} [$\log_{10}(\mathrm{Pa}\cdot\mathrm{s})$]		18.4	18.8	18.8

Note. The SUM values are shown for both 1951 and 2014, while the DUM values are only shown for 2014 as there is little variation in this layer over time. Bottom section: Elastic thickness and viscosity for the SUM and DUM of the best fitting 1D model with respect to each of the 3D/3D-s models using the 7 GPS sites ($N = 7$) a grid of points (71.25°S,80°S; 80.625°E,130°E; $N = 1{,}440$). DUM, deep upper mantle; SUM, shallow upper mantle.
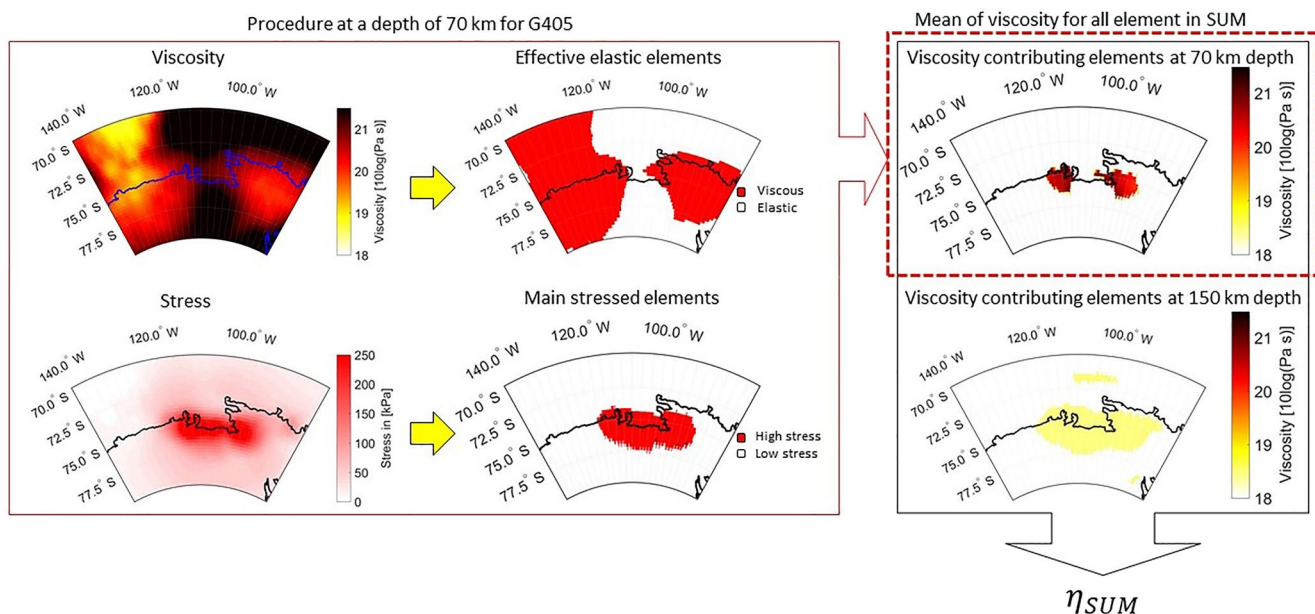

Figure 7. Schematic overview of the procedure to compute an average viscosity based on stress for the shallow upper mantle (SUM) of the G405 model. The starting values are the viscosity and the stress at any given depth (70 km in this example). The viscosity is used to determine which elements show viscous behavior (red) over the course of the simulation ($\eta < 21.0 \log_{10}(\mathrm{Pa}\cdot\mathrm{s})$). A stress threshold is used to determine the elements that contribute significantly to the uplift (red). If an element is both viscous and high-stress its viscosity is used to compute η_{SUM} together with elements that also fulfill these conditions.

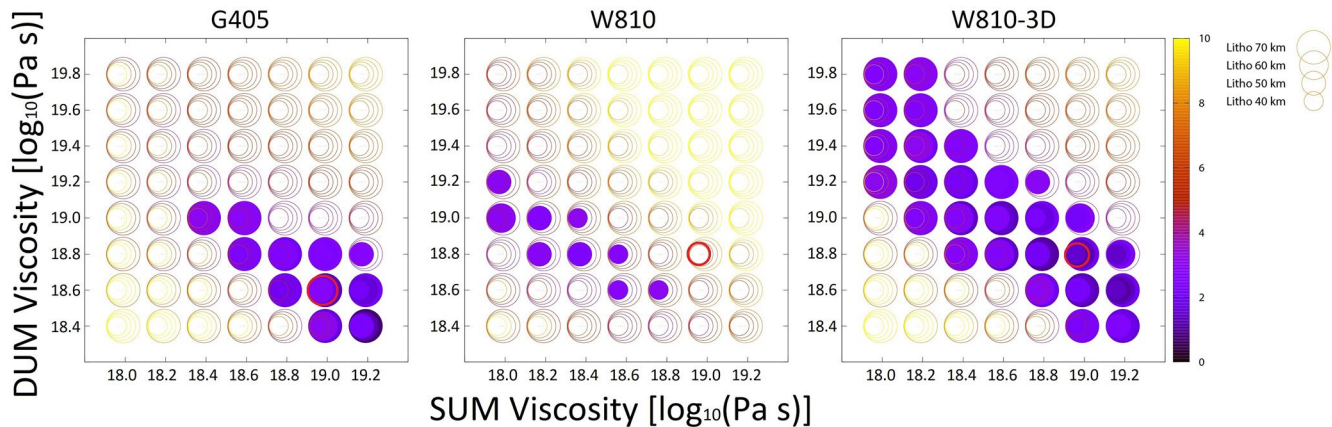**Figure 8.** χ^2 of the 1D models with respect to simulated uplift of 3D/3D-s models as a function of viscosity in the shallow upper mantle (SUM) and the deep upper mantle (DUM). Every circle is a single 1D model, with the color indicating the χ^2. The circle size denotes models with different lithospheric thickness. All solid circles represent models that fall within the 95% confidence interval. The red circle represents the average viscosity for the 3D/3D-s model.

1D and 3D/3D-s viscosity we would need additional GPS stations at specific points, or GPS stations with a lower standard deviations by for example increasing the length of the time-series. Longer time-series also open the possibility to investigate 3D-s in particular as the change in uplift over time would be visible and we might be able to identify the type of rheology under the ASE with more precision.

We now investigate whether the 1D viscosity obtained from the fit is close to the average 3D viscosity. In table 5 we see that for all three models the viscosity for the DUM is estimated to be slightly lower (maximum of 0.3 $\log_{10}(\text{Pa} \cdot \text{s})$) than the average computed from the 3D/3D-s models. For both the G405 and the W810-3D models the difference between the 1D and 3D/3D-s models in SUM viscosity is small (0.29 $\log_{10}(\text{Pa} \cdot \text{s})$ and 0.08 $\log_{10}(\text{Pa} \cdot \text{s})$). For the W810 model the SUM viscosity in the 1D model underestimates the average 3D viscosity. This means that for the W810 model both the SUM and DUM 1D estimated viscosities are lower than the average viscosity. This suggests that the uplift is determined to a larger extent by a small region of low viscosity, which is not reflected in the average viscosity. The misfit of the 1D model does not strongly depend on elastic lithosphere thickness, which becomes evident from the W810-3D case. Here the 1D model prefers a thicker lithosphere but the viscosity is still the closest possible estimate. The inversion tends to prefer thicker elastic lithosphere values for the G405. In Barletta et al. (2018) it was suggested that there could be a trade-off between upper mantle viscosity and elastic lithosphere thickness, which we see for the G405 model.

We investigate whether having limited GPS data will change the best fit 1D model with respect to the 3D/3D-s models. The best fitting model in terms of uplift is determined using 1,440 reference points (all coinciding grid-points between the models) instead of only the 7 original GPS locations (Table 5). For the G405 case there is no effect of placing more stations, as 7 stations will result in the same best fit as obtained with 1,440 stations. While this is not true for the W810 and W810-3D cases, we can still note that in these cases, the current 7 stations also give best fit models that have small differences in lithosphere thickness (10 km) or η_{SUM} (0.2 For the SUM) with respect to the best fit models with a large amount of stations. This leads us to conclude that the current 7 stations already form an adequate data set to perform inversions when determining a representative 1D viscosity.

The resolution of the FE model is fixed to the values in Table 1 and Figure 1 to limit the computation time, and interpolation is required at multiple stages, for example from the ice history data to loads applied to the finite elements or to find uplift and locations in between model nodes. To investigate the impact of this issue we have compared GPS station uplift on their exact locations, which required interpolation, as well as on the closest model nodes to these locations, requiring no interpolation. Altering the GPS locations has a small effect on the chi-square values of the best fit, but not enough to change the best fitting models in this paper. Changing interpolation methods for the computation of the gravitational perturbation changes the average uplift by approximately 0.2%. Changing the vertical resolution can have a stronger effect on the
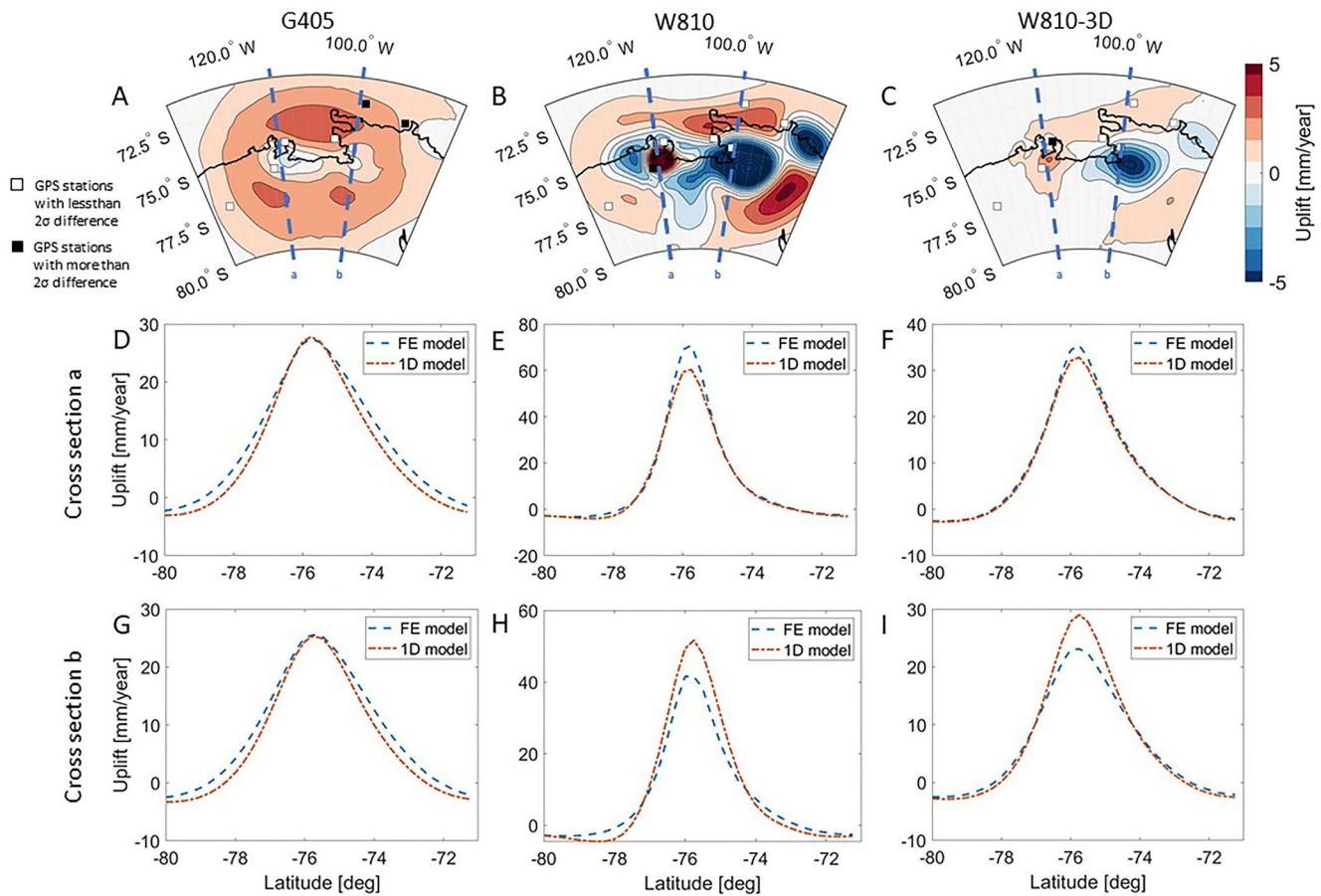
Figure 9. Top (a–c) uplift of the three models minus their best fitting 1D model. The black squares are GPS stations where the differences exceed 2σ (95% confidence), the white squares are stations where the differences are below 2σ. (d–f) cross section of the uplift of all three models and their best fitting 1D model at the 113.75 W° meridian (a), which intersects the point of maximum uplift. (g–i) cross section of the uplift of all three models and their best fitting model at the 97.5 W° meridian (b), where the differences between the three models and their best fitting 1D model are the largest.

results, because the changes in temperature in radial direction are larger than those in lateral direction. However, GIA models cannot invert uniquely for many layers, and our results are valid for the layering in the upper mantle selected for the 1D model.

3.3. 1D Versus 3D/3D-s Models Uplift

To investigate whether 1D models can represent the uplift pattern of a 3D or 3D-s model, Figure 9 shows the difference in uplift between the 3D/3D-s models and their respective best fitting 1D model. In general we can see that it is not possible for the best fit 1D models to fit any of the 3D models everywhere even though the models do not differ in a statistically significant fashion. This is because for most GPS locations the best fit 1D model uplift is close to the 3D/3D-s models uplift, although for every model there are 1 or 2 GPS stations that have a local bad fit (more than 2σ difference). Locations in between the GPS sites can still show large differences (23.1 mm/y difference for W810 and 6.7 mm/y difference for W810-3D), which is more than two times the measurement error of the GPS stations. The GIA uplift pattern, for the W810 and W810-3D model, has a sharper peak with a higher uplift than the best fitting 1D model at the point of maximum unloading (cross-section a). At 76°S in cross-section a we see more local uplift for W810 and W810-3D than the 1D model because of low local viscosity, either as consequence of the high lithosphere temperature by itself or in combination with high local stress. At cross-section b this is reversed for W810 and W810-3D, showing lower local uplift as a consequence of the local high viscosity. The different patterns

in the cross-sections show that it is not possible for a 1D model to fit the uplift pattern of the 3D/3D-s model everywhere, as a change in viscosity does not only change the magnitude of the uplift but also the spatial distribution of the uplift.

We showed earlier that more stations does little to change the best 1D model for each of the 3D/3D-s models, and that with the current data the 1D models cannot statistically be distinguished from the 3D/3D-s models. However, Figures 9b and 9c illustrate that this does not mean large differences do not exist and that with more GPS stations in the right locations 3D/3D-s differences could be detected. GPS stations at the point of maximum differences (dark red or dark blue areas) would be the most sensitive to differences between 1D models and 3D/3D-s models. For example, a GPS station in between the BERP and TOMO station (76°S 113°W, in the middle of cross section a) would be the most sensitive to possible low local viscosity. Another location that might give insight in the 3D effect is around 75.5°S 95°W (in the middle and to the right of cross section b) in Ellsworth Land. Large differences as a consequence of a high viscosity area are possibly present in this area. It must be noted that this high viscosity area is present because of the low temperature area in the WINTERC model; in the GOCE + model this area has a higher temperature which would result in a lower viscosity. These additional stations, if at all possible, at the mentioned locations, might provide us with the data to distinguish 1D, 3D, and 3D-s rheology from each other and constrain the rheological parameters to a higher accuracy. If placing extra stations is not possible another way of obtaining a data set that would be able to distinguish between rheology types is to keep the current 7 stations active for a longer time. As could already be seen in Figures 5g–5l effective viscosity changes over time under the influences of stress, which means uplift rates would change differently over time for these models compared to models with time-invariant effective viscosity. As the rheology in the ASE influences the WAIS stability it would be beneficial to extend the missions of these stations until their provided data can give us more insight in these possible non-linear components in the rheology.

3.4. Effect of Stress-Dependent Viscosity

In this section, we investigate whether 3D-s rheology gives significantly different uplift compared to 3D rheology, and if any 3D rheology can approximate the effect of 3D-s rheology. We use model W810 with varying stress, and compare it against W810 models in which stress is set to a constant level. Ideally, we would choose the Von Mises stress such that the time-averaged effective viscosity is the same, or the uplift differences are minimized as is done with the 1D model inversion. However, this is computationally expensive. Instead we use a low stress (0 kPa) and a high stress (300 kPa) as lower and upper bound, respectively. This results in a significantly higher and lower average viscosity, respectively, than computed in Table 5. We scale these uplift patterns to minimize the difference in maximum and minimum occurring uplift. The idea is that the pattern in uplift is largely fixed, but the magnitude will be changed as a function of Von Mises stress, which we reproduce by scaling the uplift. To support this idea we confirmed that upscaled results and downscaled results give a similar result (Figures 10c and 10d).

In Figure 10a, we observe that the model without stress underestimates the uplift due to the higher viscosity, while the model with 300 kPa constant stress overestimates the uplift due to the lower viscosity. The differences after scaling are positive in the center of loading and negative outside. This is the result of the constant stress models having a more spread-out uplift pattern than the 3D-s model. The average differences can not be reduced further by scaling the uplift and when computing the the χ^2_{cr} statistics for the scaled 3D models at the location of the GPS stations we obtain values of 0.23 and 0.15, respectively for the 0 KPa scaled result and the 300 KPa scaled result, which could be considered close fits. However, the 3D model still shows up to 14% less uplift at the point of maximum uplift. The higher uplift in the 3D-s model can be traced back to the viscosity decrease under the load, as stress increases (see Figures 5g–5l). It must be noted that in Figures 9a, 9d and 9g, the G405 model did not show more localized uplift despite it being a 3D-s model. That is because the G405 model was created using a smaller grain size and a lower water content, which results in a lower contribution of dislocation creep (Barnhoorn et al., 2011; Kohlstedt, 2007). In conclusion, a 3D model cannot fully reproduce the uplift from 3D-s models with significant dislocation creep, which in this case is a wet model (H_2O 1000 ppm) with a large average grain size (8 mm).
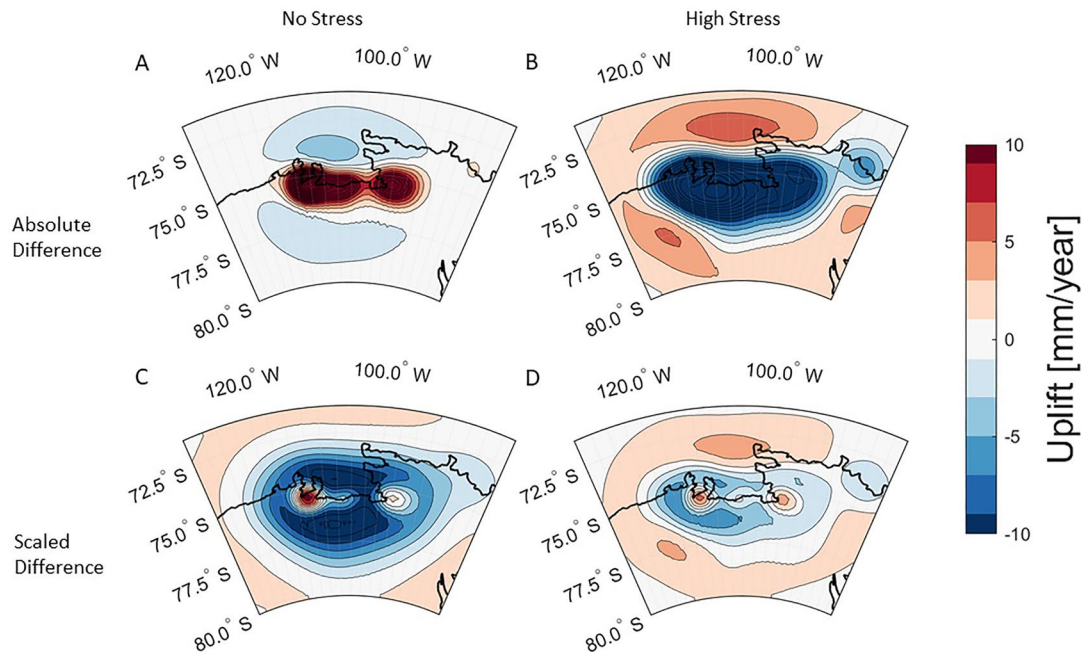
Figure 10. Differences in uplift: W810 a stress dependent viscosity minus W810 with a constant stress (and hence constant viscosity). (a and c) Difference between W810 and W810 without stress (W810-3D) induced effective viscosity changes. (b and d) Difference between W810 and W810 where a constant Von Mises stress of 300 KPa is applied. (a and b) the absolute difference between aforementioned models. (c and d) The difference when the constant stress models are scaled to minimize the differences differences, with a factor 1.73 and 0.73, for the 0 kPa case and the 300 kPa case, respectively.

Nield et al. (2018) found similar differences between 1D models and models with non-linear rheology in the Antarctic Peninsula, noting the more localized uplift in the latter, as represented by differences in gradients in uplift. An important caveat in the results presented here up until this point is that no background stresses are included. The addition of long-term GIA stresses is investigated in Section 3.5 but the interaction with stresses from other processes such as mantle convection and post-seismic deformation is left to future work.

3.5. Effect of Background Stress

In all previous evaluations we only included the effects of a recent ice history as described in Section 2.4. However, as can be seen in Equation 14 for non-linear rheology, viscosity is a function of total stress. Larger stress will increase the contribution of dislocation creep, but at the same time it might decrease the relative importance of stress changes over time due to the loading. As stated in Section 2.2, adding a background stress can either increase or decrease the change in viscosity over time due to load induced stress changes, depending on the ratio of diffusion to dislocation creep parameter. Figure 2 shows us that for a ratio of around 15 orders of magnitude between diffusion and dislocation creep parameters a small load will cause a larger reduction in viscosity than a larger load. In the G405 model the ratio between diffusion and dislocation for upper mantle elements in the ASE is between 13 and 14.5, which falls in the aforementioned window where there is a larger reduction in viscosity when loads are added with a background stress present compared to the same load case without background stress. For a wet model, such as W810, this effect is less of a issue as the ratio between diffusion and dislocation is limited between 12 and 13.5 and thus the majority of the time the reduction in viscosity is less when the load is added with a background stress compared to the case without background stress. The influence of a homogeneous background stress can be seen in Figure 11, where we look at the change in viscosity as a consequence of load induced stress. Figures 11a and 11c show a viscosity reduction similar to the viscosity change we can see in Figure 5 between 1951 and 2014. For Figures 11b and 11d a background stress of 1 Mpa is added to the load induced stress for both the G405 model and the W810 model, respectively. Only the change in stress invariant is considered here, similar to Gasperini et al. (1992) and Wu (2001).
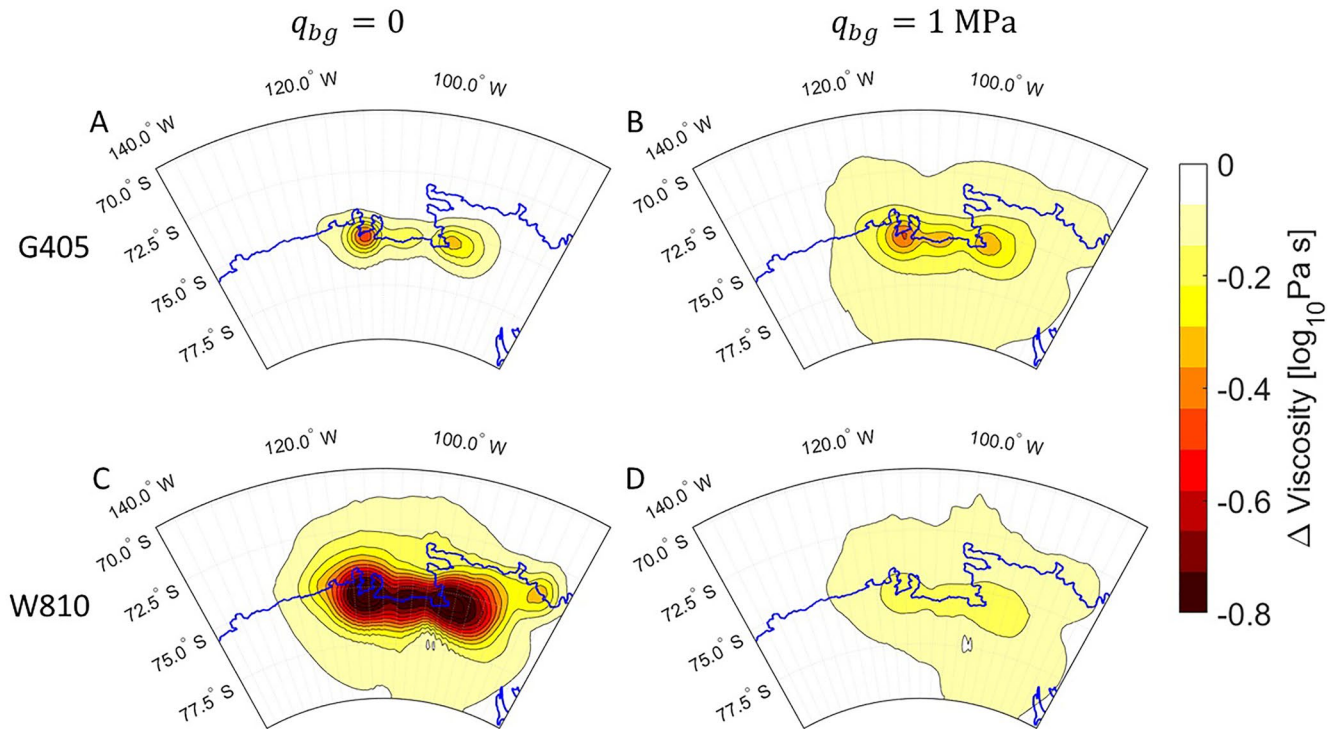
Figure 11. The change in viscosity as a consequence of load induced stress by means of dislocation creep at the end of the Amundsen Sea Embayment (ASE) simulation. (a and c) the differences in viscosity when no additional background stress is considered. (b and d) the differences when a 1 MPa background Von Mises stress is added. (aand b) both background stress cases for the G405 model. (c and d) both background stress cases for the W810 model.

The G405 model shows an increase in viscosity change when the background stress is added. Here the increasing background stress increases the importance of dislocation creep relative to diffusion creep which makes the rheology respond stronger to stress changes, as shown in Figure 2b. In the wetter W810 model the dislocation mechanism is more pronounced meaning that adding background stress will dampen the viscosity changes as a consequence of time-varying stresses.

Figure 11 is essentially a snap-shot of the present day viscosity if a background stress were to be introduced suddenly, which assumes it to be in the same principle direction as the load stresses and thus the Von Mises stress simply being the sum of both stresses. In reality a background stress field has different components, which means that the Von Mises stresses cannot be superimposed because stresses can cancel each other (Schmeling, 1987). Next we take the latent stresses from GIA as a result of the millennial scale ice load changes that occurred since the LGM as a source of background stress. We introduce this stress by running the model a full glacial cycle before the simulation enters the recent ice history as described in Section 2.4. The full glacial history assumed here is the W12 model (Whitehouse et al., 2012) which continues until 500 years B.P. although the model is an interpolation between snapshots and does not have an intrinsic 1,000 years resolution. No accounting is made for any changes in the past load-induced stresses from accumulation/ice loss changes in the interval between 0.5 and 0.1 ky, which could either decrease or increase the background stress, and could influence present uplift. Including ice change in this interval could be critical for accurate modeling of the ASE, but there is great uncertainty in how to interpret the current constrains of snow accumulation and past flux gate changes in this region of WAIS where there is such complex ice dynamics and external climate drivers. The change in viscosity as a consequence of the glacial cycle stresses can be seen in Figure 12. As a consequence of the higher viscosity in the G405 model in general more stress from the ice age loads is still present at the start of the simulation, leading to a stronger reduction in viscosity compared to W810. In W810 a larger portion of the stress has dissipated in 1900 leading to a lower viscosity drop overall. This means that while wet models have a decreased viscosity drop with background stress compared to dryer models, they also have a smaller background stress, as the ductile mantle allows those models to dissipate the stress more quickly. Both the stress itself as the reduction in viscosity strongly
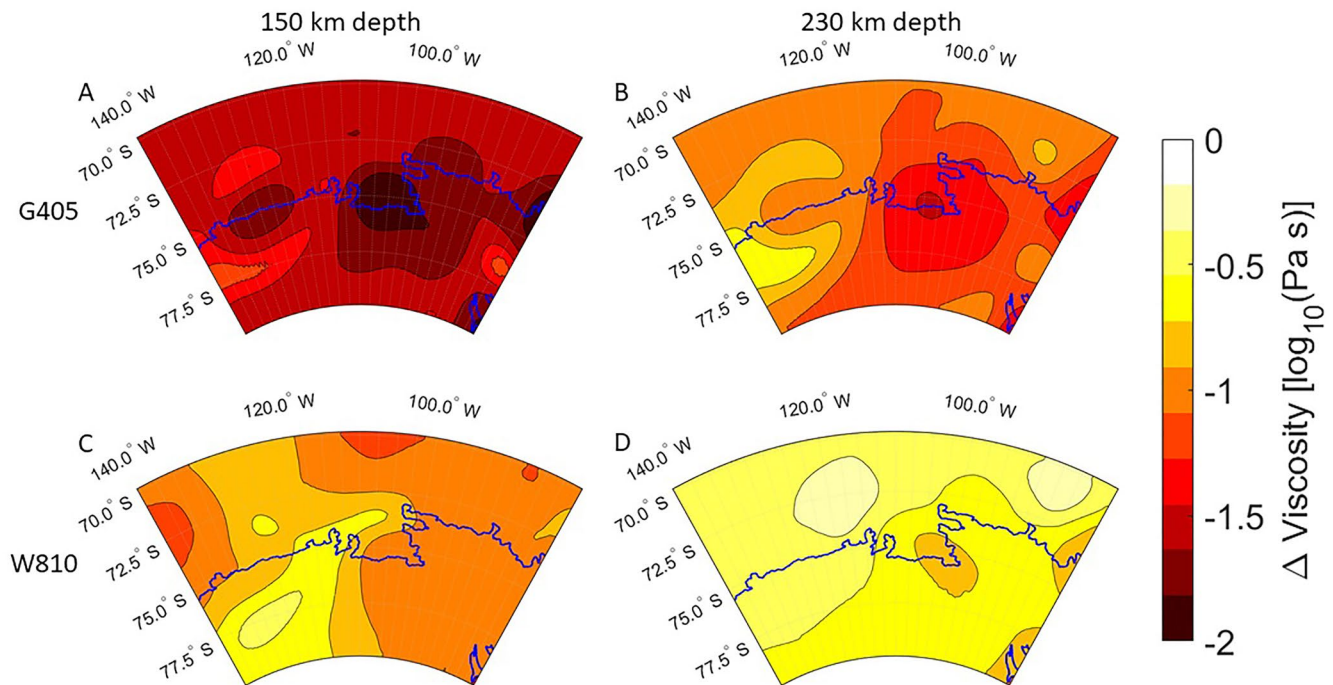
Figure 12. The change in viscosity as a consequence of ice age induced background stress by means of dislocation creep at the start of the Amundsen Sea Embayment (ASE) simulation. (a and c) the reduction in viscosity at 150 km depth. (b and d) the reduction in viscosity at 230 km depth. (a and b) Viscosity profiles at different depths with background stress present for the G405 model. (c and d) Viscosity profiles at different depths with background stress present for the W810 model.

affects the uplift for both the G405 and the W810 case. These uplift results can be seen in Figure 12. We now investigate the effect on the conclusions from Section 3.4 by comparing results with and without the inclusion of the W12 ice history (Figure 13). For G405, the uplift when a full glacial history is included, is largely determined by the ice loads from before 1900. For W810 the uplift is very similar in spatial pattern to the uplift obtained from recent ice loads, with the only difference being the increase in magnitude. The fact that the G405 is influenced by the loads before 1900 and the W810 to a lesser degree is caused by the high viscosity layer in the G405 model compared to the W810 model. This high viscosity layer is still stressed at the end of the simulation from ice loads predating 1900. However, high viscosity models are unlikely given the good fit Barletta et al. (2018) achieved only considering recent ice changes. In order to understand the effect ice age stress has on current day uplift through changes in viscosity, the non-linear component in the uplift was computed by combining the uplift from recent ice mass changes with the uplift from the ice age simulation (so there is no stress interaction) and subtract those from a single simulation where both ice histories are present (where there is stress interaction). For W810 we see that the pattern of the non-linear component matches both the uplift as a consequence of the current ice mass changes as well as the uplift from the combined ice history. If we scale the results of the combined simulation to match the results that only include recent ice changes, the resulting difference is very low. From this we can conclude that for wet models or models with low viscosity in general, background stress can have a significant effect on the total uplift as a consequence of an overall lowering in viscosity, even more so considering stress from ice mass loss in the centuries before 1900. However, as a significant portion of the background stress dissipates quickly, especially for regions that have high local stress, the overall effect on the spatial uplift pattern is limited. Areas that have experienced recent high load changes will still have more localized uplift compared to 3D and 1D models. For G405 the situation is different as the high amount of stress in the mantle present at 1900 both changes the viscosity and local Von Mises stress such that non-linear component does not show a straight forward magnitude change in the uplift, but instead even shows areas where the non-linear component is negative. In these area's background stress and recent ice load stress have canceled each other to some degree. The conclusion here is that for high viscosity or dryer areas, where one might expect the role of stress over time to be limited considering the small contribution of dislocation creep, non-linear rheology
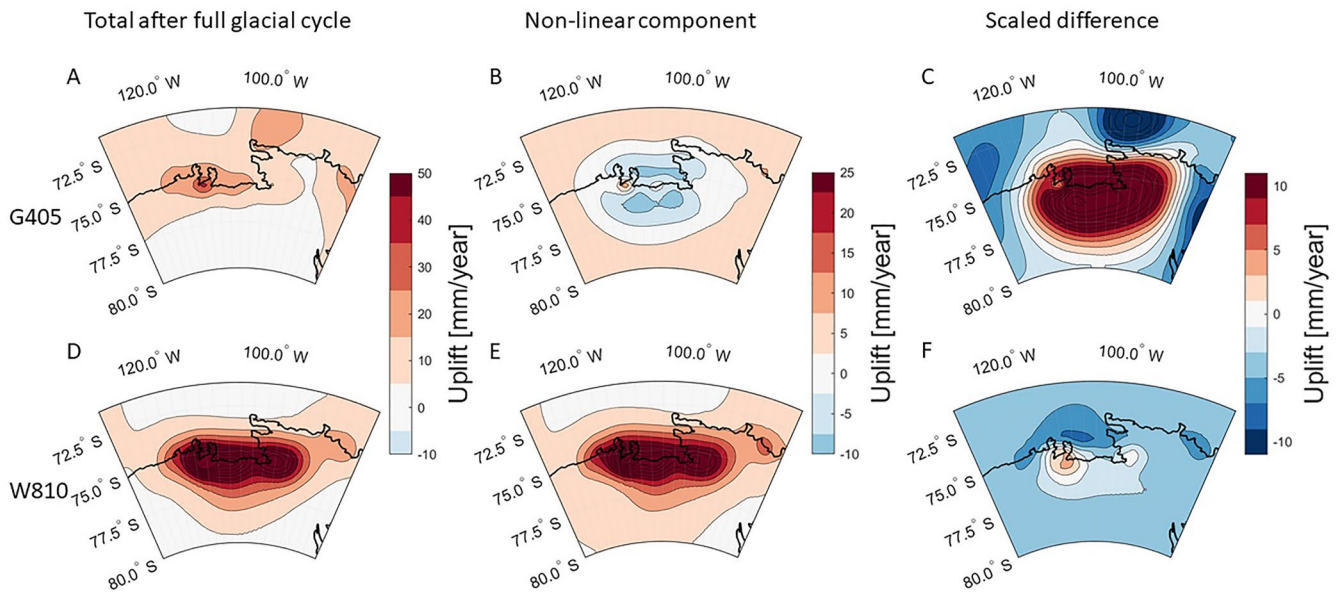
Figure 13. (a and d) uplift for both the G405 model (a) and the W810 model (d) when loaded with the W12 ice history as well as the recent ice history from Figure 4. (b and e) The difference between the uplift of full glaciale cycle with recent loads combined in a single run and the uplift of both of those components in separate runs. This is the uplift as a consequence of the non-linear component in the rheology. (c and f) the uplift of the models without glacial history are scaled such that the differences squared as shown in the central column are minimized.

can still have a large impact on the final results. Even though changes in viscosity over short time frames will be less likely for these cases, the high viscosity means that stress will linger for a longer time which increases the chance of stress from different processes or time periods to interact and affect viscosity. As a consequence of the overall lowered viscosity the uplift response at present is stronger.

4. Conclusions

In the ASE region there is evidence for varying mantle structure which manifests as viscosity variations of one order of magnitude. Given the importance of dislocation creep in mantle deformation, it is also possible that stress changes induce viscosity changes over time and space. We label the model with stress-dependent viscosity as "3D-s." Note that this still constitutes Maxwell rheology with steady-state creep. We did not include transient creep as simulated by a Burgers rheology. We simulate uplift with two different 3D-s models and a 3D model with olivine rheology with varying grain size, water content and spatial variations as a function of temperature and stress. We perform a 1D model inversion for the uplift of these models to find out how close the 1D model predictions are to those of the 3D/3D-s models.

We investigate two different temperature models based on inversion of the petrophysical-geophysical framework LitMod, with one largely based on gravity data (GOCE+) leading to more spatially homogeneous temperature and higher viscosity, and the other relying more on seismic data (WINTERC 3.2), resulting in lower viscosity and more spatial variations. For each temperature model, rheological parameters from a limited range are taken which best fit GPS uplift in the ASE. The first of the three models, G405 is based on the GOCE + temperature profile, has a small grain size of 4 mm and a rheology between fully wet and dry olivine. The effective viscosity is rather homogeneous and has a small 3D-s effect, only dropping 0.2–0.4 $\log_{10}(\text{Pa} \cdot \text{s})$ directly under the maximum load in the last half century. The second model, W810, is based on WINTERC 3.2 and has a large grain size of 8 mm and fully wet rheology. For the latter model stress-dependence can be switched off by prescribing stress to be constant. This model is refered as W810-3D

The first main conclusion is that the best-fitting viscosity in the 1D models is close (difference of 0.3 $\log_{10}$ (Pa · s) maximum) to the average viscosity of the 3D and 3D-s models in the upper mantle between 200 and 400 km. At this depth the influence of 3D and 3D-s variations is small. For the viscosity estimate of

depths shallower than 200 km the best fitting 1D models also find good viscosity estimates for the models with low to no stress induced variations over time in the effective viscosity. However, for W810, where stress changes reduce local viscosity more significantly, the 1D viscosity does not represent the wider regional viscosity, but is biased toward local viscosity at present underneath the largest mass changes. In that case, differences in average viscosity between the standard set by W810 and the best fitting 1D model can be more than half an order of magnitude. Recent studies demonstrating abnormally low viscosity underneath the ASE are probably giving a reasonable reflection of a weighted average of a current 3D viscosity structure in the region with a stronger influence from the low viscosities under the sites of the largest mass changes.

We found that the differences between 1D and 3D models in uplift are possibly significant depending on the locations in the ASE and the 3D model assumed. This is somewhat in contrast to Powell et al. (2020), who state that 1D and 3D differences will exceed GPS measurement errors in the future but finds that for the present day the difference between regionally adapted 1D models and 3D models are around the magnitude of the measurement error and smaller. However, they did not include non-linear rheology, which as shown in this study can increase difference with 1D models significantly and had a shorter ice history, which starts from a steady-state in 1992 instead of 1900. We do find that 1D models are able to fit the current regional ASE set of uplift rate measurements to a statistically significant degree and are indistinguishable from 3D/3D-s models. Despite this, this study also shows that it is also possible with certain rheologies that locations can be identified where 1D models exceed the GPS measurement error and can be distinguished from 3D/3D-s models.

For 3D-s models, the stress-dependence of viscosity creates a temporary region of low viscosity below the load. This makes uplift patterns more local for the 3D-s model compared to the 1D and 3D model. The uplift near the point of maximum stress is underestimated by the best fitting 1D model, while uplift in surrounding areas and the collapse of the forebulge is overestimated; the 1D model cannot fit both regions simultaneously. If 1D models are used to correct GIA effect in mass change measurements it could mean that GIA derived gravity rate is too low at the area of maximum mass loss and too large elsewhere. However, this result is sensitive to the magnitude of ice load changes and even more to the presence of background stresses.

When including background stresses, such as a full glacial cycle, the load induced effective viscosity drop can be amplified or weakened, depending on the relative importance of diffusion and dislocation creep. A dryer model, such as the G405 model falls within the category for which including background stress increases these viscosity drops. Due to a high viscosity in the upper mantle, G405 showed uplift patterns that were influenced by stress changes due to ice mass changes from before 1900, while the low viscosity upper mantle of the W810 model meant that stresses from earlier deglaciation were already decayed. From Barletta et al. (2018) we know that observed uplift can be modeled to a high degree by only using the recent ice history. This indicates that a low viscosity mantle such as in the W810 or W810-3D model is more likely to be representative of the actual mantle underneath the ASE. However, for both the G405 model as well as the W810 model the inclusion of stress from the LGM ice loads did change the uplift result significantly, suggesting that background stresses have to be included in areas of large past ice load changes. This likely also holds for stress in the period before recent ice melt that is not included in our model. Mass increase or decrease in the pre-1900 woud influence viscosity, especially for the lower viscosity model. Stresses due to LGM ice load changes can be similar to or smaller than those of mantle convection. In the presence of large mantle convection induced background stress, the effect of 3D-s rheology used in this study is even more unpredictable. As the background stress could be spatially uncorrelated to the ice load induced stresses. The effect of mantle induced background stress is an important topic for future study.

Data Availability Statement

All model generated data used in this study can be found at data.4tu.nl under https://doi.org/10.4121/14872266.

References

A, G., Wahr, J., & Zhong, S. (2013). Computations of the viscoelastic response of a 3-D compressible Earth to surface loading: An application to glacial isostatic adjustment in Antarctica and Canada. *Geophysical Journal International*, *192*(2), 557–572. https://doi.org/10.1093/gji/ggs030

Afonso, J. C., Fernàndez, M., Ranalli, G., Griffin, W. L., & Connolly, J. A. D. (2008). Integrated geophysical-petrological modeling of the lithosphere and sublithospheric upper mantle: Methodology and applications. *Geochemistry, Geophysics, Geosystems*, *9*(5). https://doi.org/10.1029/2007gc001834

An, M., Wiens, D. A., Zhao, Y., Feng, M., Nyblade, A. A., Kanao, M., et al. (2015a). S-velocity model and inferred Moho topography beneath the Antarctic Plate from Rayleigh waves. *Journal of Geophysical Research: Solid Earth*, *120*(1), 359–383. https://doi.org/10.1002/2014jb011332

An, M., Wiens, D. A., Zhao, Y., Feng, M., Nyblade, A., Kanao, M., et al. (2015b). Temperature, lithosphere-asthenosphere boundary, and heat flux beneath the Antarctic Plate inferred from seismic velocities. *Journal of Geophysical Research: Solid Earth*, *120*(12), 8720–8742. https://doi.org/10.1002/2015jb011917

Barletta, V., Bevis, M., Smith, B., Wilson, T., Brown, A., Bordoni, A., et al. (2018). Observed rapid bedrock uplift in Amundsen Sea Embayment promotes ice-sheet stability. *Science*, *360*(6395), 1335–1339. https://doi.org/10.1126/science.aao1447

Barnhoorn, A., van der Wal, W., Vermeersen, B. L. A., & Drury, M. R. (2011). Lateral, radial, and temporal variations in upper mantle viscosity and rheology under Scandinavia. *Geochemistry, Geophysics, Geosystems*, *12*(1). https://doi.org/10.1029/2010gc003290

Carcione, J. M., Poletto, F., Farina, B., & Craglietto, A. (2014). Simulation of seismic waves at the earth's crust (brittle–ductile transition) based on the burgers model. *Solid Earth*, *5*(2), 1001–1010. https://doi.org/10.5194/se-5-1001-2014. Retrieved from https://se.copernicus.org/articles/5/1001/2014/

Caron, L., & Ivins, E. R. (2020). A baseline Antarctic GIA correction for space gravimetry. *Earth and Planetary Science Letters*, *531*, 115957. https://doi.org/10.1016/j.epsl.2019.115957

Dziewonski, A. M., & Anderson, D. L. (1981). Preliminary reference Earth model. *Physics of the Earth and Planetary Interiors*, *25*(4), 297–356. https://doi.org/10.1016/0031-9201(81)90046-7

Eagles, G., Gohl, K., & Larter, R. D. (2009). Animated tectonic reconstruction of the southern pacific and alkaline volcanism at its convergent margins since Eocene times. *Tectonophysics*, *464*(1–4), 21–29. https://doi.org/10.1016/j.tecto.2007.10.005

Eagles, G., Larter, R. D., Gohl, K., & Vaughan, A. P. (2009). West Antarctic rift system in the Antarctic Peninsula. *Geophysical Research Letters*, *36*(21). https://doi.org/10.1029/2009gl040721

Fullea, J., Afonso, J. C., Connolly, J. A. D., Fernàndez, M., García-Castellanos, D., & Zeyen, H. (2009). LitMod3D: An interactive 3D software to model the thermal, compositional, density, seismological, and rheological structure of the lithosphere and sublithospheric upper mantle. *Geochemistry, Geophysics, Geosystems*, *10*(8). https://doi.org/10.1029/2009gc002391

Fullea, J., Lebedev, S., Martinec, Z., & Celli, N. L. (2018). *WINTERC: A new global thermochemical model constrained by seismic waveforms, heat flow, surface elevation and gravity satellite data*.

Gardner, A. S., Moholdt, G., Scambos, T., Fahnstock, M., Ligtenberg, S., Broeke, M. v. d., & Nilsson, J. (2018). Increased west Antarctic and unchanged east Antarctic ice discharge over the last 7 years. *The Cryosphere*, *12*(2), 521–547. https://doi.org/10.5194/tc-12-521-2018

Gasperini, P., Yuen, D. A., & Sabadini, R. (1992). Postglacial rebound with a non-Newtonian upper mantle and a Newtonian lower mantle rheology. *Geophysical Research Letters*, *19*(16), 1711–1714. https://doi.org/10.1029/92gl01456

Gomez, N., Latychev, K., & Pollard, D. (2018). A Coupled ice sheet–sea level model incorporating 3D Earth structure: Variations in Antarctica during the last deglacial retreat. *Journal of Climate*, *31*(10), 4041–4054. https://doi.org/10.1175/jcli-d-17-0352.1

Gourmelen, N., Escorihuela, M., Shepherd, A., Foresta, L., Muir, A., Garcia-Mondéjar, A., et al. (2018). CryoSat-2 swath interferometric altimetry for mapping ice elevation and elevation change. *Advances in Space Research*, *62*(6), 1226–1242. https://doi.org/10.1016/j.asr.2017.11.014

Hartmann, R., Ebbing, J., & Conrad, P. (2020). A Multiple 1D Earth Approach (M1DEA) to account for lateral viscosity variations in solutions of the sea level equation: An application for glacial isostatic adjustment by Antarctic deglaciation. *Journal of Geodynamics*, *135*. https://doi.org/10.1016/j.jog.2020.101695

Hay, C. C., Lau, H. C. P., Gomez, N., Austermann, J., Powell, E., Mitrovica, J. X., et al. (2017). Sea level fingerprints in a region of complex earth structure: The case of WAIS. *Journal of Climate*, *30*(6), 1881–1892. https://doi.org/10.1175/jcli-d-16-0388.1

Hirth, G., & Kohlstedt, D. (2003). Rheology of the upper mantle and the mantle wedge: A view from the experimentalists. *Geophysical Monograph-American Geophysical Union*, *138*, 83–105. https://doi.org/10.1029/138gm06

Hirth, G., & Kohlstedt, D. (2015). The stress dependence of olivine creep rate: Implications for extrapolation of lab data and interpretation of recrystallized grain size. *Earth and Planetary Science Letters*, *418*, 20–26. https://doi.org/10.1016/j.epsl.2015.02.013. Retrieved from https://www.sciencedirect.com/science/article/pii/S0012821X15000916

Hu, H., van der Wal, W., & Vermeersen, L. L. A. (2017). A numerical method for reorientation of rotating tidally deformed viscoelastic bodies. *Journal of Geophysical Research: Planets*, *122*(1), 228–248. https://doi.org/10.1002/2016je005114

Huang, P., Wu, P., & Steffen, H. (2019). In search of an ice history that is consistent with composite rheology in Glacial Isostatic Adjustment modelling. *Earth and Planetary Science Letters*, *517*, 26–37. https://doi.org/10.1016/j.epsl.2019.04.011

Ivins, E. R., Caron, L., Adhikari, S., Larour, E., & Scheinert, M. (2020). A linear viscoelasticity for decadal to centennial time scale mantle deformation. *Reports on Progress in Physics*, *83*(10), 106801. https://doi.org/10.1088/1361-6633/aba346

Ivins, E. R., James, T. S., Wahr, J., Schrama, E. J. O., Landerer, F. W., & Simon, K. M. (2013). Antarctic contribution to sea level rise observed by GRACE with improved GIA correction. *Journal of Geophysical Research: Solid Earth*, *118*(6), 3126–3141. https://doi.org/10.1002/jgrb.50208

Ivins, E. R., Raymond, C. A., & James, T. S. (2000). The influence of 5000 year-old and younger glacial mass variability on present-day crustal rebound in the Antarctic peninsula. *Earth Planets and Space*, *52*(11), 1023–1029. https://doi.org/10.1186/bf03352325

Ivins, E. R., Raymond, C. A., & James, T. S. (2002). Late-pleistocene, holocene and present-day ice load evolution in the Antarctic peninsula: Models and predicted vertical crustal motion. *Ice Sheets, Sea Level and the Dynamic Earth*, *29*, 133–155. https://doi.org/10.1029/gd029p0133

Ivins, E. R., van der Wal, W., Wiens, D., Lloyd, A., & Caron, L. (2021). *Antarctic upper mantle rheology*. Geological society of London Memoir.

Jackson, I., & Faul, U. H. (2010). Grainsize-sensitive viscoelastic relaxation in olivine: Towards a robust laboratory-based model for seismological application. *Physics of the Earth and Planetary Interiors*, *183*(1), 151–163. https://doi.org/10.1016/j.pepi.2010.09.005

Johnston, P. (1993). The effect of spatially non-uniform water loads on prediction of sea-level change. *Geophysical Journal International*, *114*(3), 615–634. https://doi.org/10.1111/j.1365-246x.1993.tb06992.x

Kaufmann, G., Wu, P., & Ivins, E. (2005). Lateral viscosity variations beneath Antarctica and their implications on regional rebound motions and seismotectonics. *Geophysics Journal International*, *161*, 679–706. https://doi.org/10.1016/j.jog.2004.08.009

Kearey, P., Klepeis, K. A., & Vine, F. J. (2009). *Global tectonics* (3rd ed.). Wiley–Blackwell.

Kendall, R. A., Mitrovica, J. X., & Milne, G. A. (2005). On post-glacial sea level - II. Numerical formulation and comparative results on spherically symmetric models. *Geophysics Journal International*, *161*, 679–706. https://doi.org/10.1111/j.1365-246x.2005.02553.x

King, M. A., Altamimi, Z., Boehm, J., Bos, M., Dach, R., Elosegui, P., et al. (2010). Improved constraints on models of glacial isostatic adjustment: A Review of the contribution of ground-based geodetic observations. *Surveys in Geophysics*, *31*, 465–507. https://doi.org/10.1007/s10712-010-9100-4

Kohlstedt, D. (2007). Properties of rocks and minerals–constitutive equations, rheological behavior, and viscosity of rocks. In: *Treatise on geophysics* (pp. 389–417). Elsevier. https://doi.org/10.1016/b978-044452748-6/00043-2

Konrad, H., Gilbert, L., Cornford, S. L., Payne, A., Hogg, A., Muir, A., & Shepherd, A. (2016). Uneven onset and pace of ice-dynamical imbalance in the Amundsen Sea Embayment, West Antarctica. *Geophysical Research Letters*, *44*(2), 910–918.

Konrad, H., Sasgen, I., Pollard, D., & Klemann, D. (2015). Potential of the solid-Earth response for limiting long-term West Antarctic Ice Sheet retreat in a warming climate. *Earth and Planetary Science Letters*, *432*(15), 254–264. https://doi.org/10.1016/j.epsl.2015.10.008

Lau, H. C., & Holtzman, B. K. (2019). "Measures of dissipation in viscoelastic media" extended: Toward continuous characterization across very broad geophysical time scales. *Geophysical Research Letters*, *46*(16), 9544–9553. https://doi.org/10.1029/2019gl083529

Lau, H. C., Holtzman, B. K., & Havlin, C. (2020). Toward a self-consistent characterization of lithospheric plates using full-spectrum viscoelasticity. *AGU Advances*, *1*(4), e2020AV000205. https://doi.org/10.1029/2020av000205

Liu, B., King, M., & Dai, W. (2018). Common mode error in Antarctic GPS coordinate time-series on its effect on bedrock-uplift estimates. *Geophysics Journal International*, *214*(3), 1652–1664. https://doi.org/10.1093/gji/ggy217

Lloyd, A. J., Wiens, D. A., Nyblade, A. A., Anandakrishnan, S., Aster, R. C., Huerta, A. D., et al. (2015). A seismic transect across West Antarctica: Evidence for mantle thermal anomalies beneath the Bentley Subglacial Trench and the Marie Byrd Land Dome. *Journal of Geophysical Research: Solid Earth*, *120*(12), 8439–8460. https://doi.org/10.1002/2015jb012455

Martinec, Z., Klemann, V., van der Wal, W., Riva, R. E. M., Spada, G., Sun, Y., et al. (2018). A benchmark study of numerical implementations of the sea level equation in GIA modelling. *Geophysical Journal International*, *215*, 389–414. https://doi.org/10.1093/gji/ggy280

Martín-Español, A., King, M., Zammit-Mangion, A., Andrews, S., Moore, P., & Bamber, J. (2016). An assessment of forward and inverse GIA solutions for Antarctica. *Journal of Geophysical Research: Solid Earth*, *121*, 6947–6965.

McDonough, W., & Sun, S.-S. (1995). The composition of the Earth. *Chemical Geology*, *120*(3), 223–253. https://doi.org/10.1016/0009-2541(94)00140-4

Milne, G. A., & Mitrovica, J. X. (1998). The influence of time-dependent ocean-continent geometry on predictions of post-glacial sea level change in Australia and New Zealand. *Geophysical Research Letters*, *25*(6), 793–796. https://doi.org/10.1029/98gl00498

Mouginot, J., Rignot, E., & Scheuchl, B. (2014). Sustained increase in ice discharge from the Amundsen Sea Embayment, West Antarctica, from 1973 to 2013. *Geophysical Research Letters*, *41*(5). https://doi.org/10.1002/2013gl059069

Nield, G. A., Barletta, V. R., Bordoni, A., King, M. A., Whitehouse, P. L., Clarke, P. J., et al. (2014). Rapid bedrock uplift in the Antarctic Peninsula explained by viscoelastic response to recent ice unloading. *Earth and Planetary Science Letters*, *397*(2), 32–41. https://doi.org/10.1016/j.epsl.2014.04.019

Nield, G. A., King, M. A., Steffen, R., & Blank, B. (2020). A global, spherical, finite-element model for postseismic deformation using abaqus. *Geoscientific Model Development Discussions*, [preprint] 1–18.

Nield, G. A., Whitehouse, P. L., van der Wal, W., Blank, B., O'Donnell, J. P., & Stuart, G. W. (2018). The impact of lateral variations in lithospheric thickness on glacial isostatic adjustment in West Antarctica. *Geophysics Journal International*, *214*(2), 811–824. https://doi.org/10.1093/gji/ggy158

Pappa, F., Ebbing, J., Ferraccioli, F., & van der Wal, W. (2019). Modeling satellite gravity gradient data to derive density, temperature, and viscosity structure of the Antarctic lithosphere. *JGR Solid Earth*, *124*(11). https://doi.org/10.1029/2019jb017997

Peltier, W. (2004). Global glacial isostasy and the surface of the ice-age Earth: The ICE-5G (VM2) Model and GRACE. *Annual Review of Earth and Planetary Sciences*, *32*(1), 111–149. https://doi.org/10.1146/annurev.earth.32.082503.144359

Powell, E., Gomez, N., Hay, C., Latychev, K., & Mitrovica, J. X. (2020). Viscous effects in the solid Earth response to modern Antarctic ice mass flux: Implications for geodetic studies of WAIS stability in a warming world. *Journal of Climate*, *33*(2), 443–459. https://doi.org/10.1175/jcli-d-19-0479.1

Ranalli, G. (1995). *Rheology of the earth*. Cambridge University Press.

Rignot, E., Mouginot, J., Scheuchl, B., Van Den Broeke, M., Van Wessem, M. J., & Morlighem, M. (2019). Four decades of Antarctic ice sheet mass balance from 1979–2017. *Proceedings of the National Academy of Sciences*, *116*(4), 1095–1103. https://doi.org/10.1073/pnas.1812883116

Samrat, N. H., King, M. A., Watson, C., Hooper, A., Chen, X., Barletta, V. R., & Bordoni, A. (2020). Reduced ice mass loss and three-dimensional viscoelastic deformation in northern Antarctic Peninsula inferred from GPS. *Geophysical Journal International*, *222*(2), 1013–1022. https://doi.org/10.1093/gji/ggaa229

Schaeffer, A. J., & Lebedev, S. (2013). Global shear speed structure of the upper mantle and transition zone. *Geophysical Journal International*, *194*(1), 417–449. https://doi.org/10.1093/gji/ggt095

Schmeling, H. (1987). On the interaction between small- and large-scale convection and postglacial rebound flow in a power-law mantle. *Earth and Planetary Science Letters*, *84*(2), 254–262. https://doi.org/10.1016/0012-821x(87)90090-2

Seroussi, H., Nakayama, Y., Larour, E., Menemenlis, D., Morlighem, M., Rignot, E., & Khazendar, A. (2017). Continued retreat of Thwaites glacier, West Antarctica, controlled by bed topography and ocean circulation. *Geophysical Research Letters*, *44*(12), 6191–6199. https://doi.org/10.1002/2017gl072910

Shen, W., Wiens, D. A., Lloyd, A. J., & Nyblade, A. A. (2020). A geothermal heat flux map of Antarctica empirically constrained by seismic structure. *Geophysical Research Letters*, *47*(14), GL086955. https://doi.org/10.1029/2020gl086955

Shepherd, A., Gilbert, L., Muir, H., Alan, S., Konrad, H., McMillan, M., et al. (2019). Trends in Antarctic Ice Sheet elevation and mass. *Geophysical Research Letters*, *46*(14), 8174–8183. https://doi.org/10.1029/2019gl082182

Shepherd, A., Ivins, E., Rignot, E., Smith, B., Van Den Broeke, M., & Velicogna, I. (2018). Mass balance of the Antarctic ice sheet from 1992 to 2017. *Nature*, *558*, 219–222. https://doi.org/10.1038/s41586-018-0179-y

Spada, G., Barletta, V. R., Klemann, V., Riva, R. E. M., Martinec, Z., Gasperini, P., et al. (2011). A benchmark study for glacial isostatic adjustment codes. *Geophysical Journal International*, *185*(1), 106–132. https://doi.org/10.1111/j.1365-246x.2011.04952.x

van der Wal, W., Barnhoorn, A., Stocchi, P., Gradmann, S., Wu, P., Drury, M., & Vermeersen, B. (2013). Glacial isostatic adjustment model with composite 3-D Earth rheology for Fennoscandia. *Geophysical Journal International*, *194*, 61–77. https://doi.org/10.1093/gji/ggt099

van der Wal, W., Whitehouse, P. L., & Schrama, E. J. (2015). Effect of the GIA models with 3D composite mantle viscosity on GRACE mass balance estimates for Antarctica. *Earth and Planetary Science Letters*, *414*, 134–143. https://doi.org/10.1016/j.epsl.2015.01.001

van der Wal, W., Wu, P., Wang, H., & Sideris, M. G. (2010). Sea levels and uplift rate from composite rheology in glacial isostatic adjustment modeling. *Journal of Geodynamics*, *50*(1), 38–48. https://doi.org/10.1016/j.jog.2010.01.006

Whitehouse, P. L., Bentley, M. J., Milne, G. A., King, M. A., & Thomas, I. D. (2012). A new glacial isostatic adjustment model for Antarctica: Calibrated and tested using observations of relative sea-level change and present-day uplift rates. *Geophysical Journal International*, *190*(3), 1464–1482. https://doi.org/10.1111/j.1365-246x.2012.05557.x

Whitehouse, P. L., Gomez, N., King, M. A., & Wiens, D. A. (2019). Solid Earth change and the evolution of the Antarctic Ice Sheet. *Nature Communications*, *10*(503). https://doi.org/10.1038/s41467-018-08068-y

Wolstencroft, M., King, M. A., Whitehouse, P. L., Bentley, M. J., Nield, G. A., King, E. C., et al. (2015). Uplift rates from a new high-density GPS network in Palmer Land indicate significant late Holocene ice loss in the southwestern Weddell Sea. *Geophysical Journal International*, *203*(1), 737–754. https://doi.org/10.1093/gji/ggv327

Wong, M. C., & Wu, P. (2019). Using commercial finite-element packages for the study of glacial isostatic adjustment on a compressible self-gravitating spherical Earth–1: Harmonic loads. *Geophysical Journal International*, *217*(3), 1798–1820. https://doi.org/10.1093/gji/ggz108

Wu, P. (2001). Postglacial induced surface motion and gravity in Laurentia for uniform mantle with power-law rheology and ambient tectonic stress. *Earth and Planetary Science Letters*, *186*(3), 427–435. https://doi.org/10.1016/s0012-821x(01)00258-8

Wu, P. (2004). Using commercial finite element packages for the study of the earth deformations, sea levels and the state of stress. *Geophysics Journal International*, *158*, 401–408. https://doi.org/10.1111/j.1365-246x.2004.02338.x

Zhang, R. (2005). *Numerical simulation of solid-state sintering of metal powder compact dominated by grain boundary diffusion (unpublished doctoral dissertation)*. Penn State.